Kinematics of the O VI Circumgalactic Medium: Halo Mass Dependence and Outflow Signatures

Ng, M.; Nielsen, N.M.; Kacprzak, G.G.; Pointon, S.K.; Muzahid, S.; Churchill, C.W.; Charlton, J.C.

arXiv:1904.08564v1 [astro-ph.GA] 18 Apr 2019

KINEMATICS OF THE O VI CIRCUMGALACTIC MEDIUM: HALO MASS DEPENDENCE AND OUTFLOW SIGNATURES

Mason Ng[1,2,†], Nikole M. Nielsen[1], Glenn G. Kacprzak[1,3], Stephanie K. Pointon[1,3], Sowgat Muzahid[4,5], Christopher W. Churchill[6], and Jane C. Charlton[4],

[1] Centre for Astrophysics and Supercomputing, Swinburne University of Technology, Hawthorn, Victoria 3122, Australia
[2] Research School of Astronomy and Astrophysics, Australian National University, ACT 2611, Australia
[3] ARC Centre of Excellence for All Sky Astrophysics in 3 Dimensions (ASTRO 3D), Australia
[4] Department of Astronomy & Astrophysics, The Pennsylvania State University, State College, PA 16801, USA
[5] Leiden Observatory, Leiden University, PO Box 9513, NL-2300 RA Leiden, The Netherlands
[6] Department of Astronomy, New Mexico State University, Las Cruces, NM 88003, USA
Draft version April 19, 2019

ABSTRACT

We probe the high-ionization circumgalactic medium by examining absorber kinematics, absorber–galaxy kinematics, and average absorption profiles of 31 O VI absorbers from the "Multiphase Galaxy Halos" Survey as a function of halo mass, redshift, inclination, and azimuthal angle. The galaxies are isolated at $0.12 < z_{gal} < 0.66$ and are probed by a background quasar within $D \approx 200$ kpc. Each absorber–galaxy pair has *Hubble Space Telescope* images and COS quasar spectra, and most galaxy redshifts have been accurately measured from Keck/ESI spectra. Using the pixel-velocity two-point correlation function (TPCF) method, we find that O VI absorber kinematics have a strong halo mass dependence. Absorbers hosted by $\sim L^*$ galaxies have the largest velocity dispersions, which we interpret to be that the halo virial temperature closely matches the temperature at which the collisionally ionized O VI fraction peaks. Lower mass galaxies and group environments have smaller velocity dispersions. Total column densities follow the same behavior, consistent with theoretical findings. After normalizing out the observed mass dependence, we studied absorber–galaxy kinematics with a modified TPCF and found non-virialized motions due to outflowing gas. Edge-on minor axis gas has large optical depths concentrated near the galaxy systemic velocity as expected for bipolar outflows, while face-on minor axis gas has a smoothly decreasing optical depth distribution out to large normalized absorber–galaxy velocities, suggestive of decelerating outflowing gas. Accreting gas signatures are not observed due to "kinematic blurring" in which multiple line-of-sight structures are observed. These results indicate that galaxy mass dominates O VI properties over baryon cycle processes.

Keywords: galaxies: halos — quasars: absorption lines

1. INTRODUCTION

The prodigious reserves of gas surrounding galaxies in the circumgalactic medium (CGM) play an important role in galaxy evolution (see review by Tumlinson et al. 2017). This gas is primarily derived from the intergalactic medium (IGM, e.g., Putman et al. 2012; Cooper et al. 2015; Glidden et al. 2016), from cannibalizing satellite galaxies (e.g., Cole et al. 2000; Cox et al. 2008; Qu et al. 2011; Lambas et al. 2012a,b; Kaviraj 2014; Ownsworth et al. 2014; Gómez-Guijarro et al. 2018), and from galactic feedback (e.g., Strickland & Heckman 2009; Schaye et al. 2015; van de Voort 2017; Butler et al. 2017; Correa et al. 2018). The general accepted picture of how a typical galaxy evolves includes the accretion of relatively metal-poor gas from the CGM onto the galactic disk (see review by Kacprzak 2017), which is used to fuel star formation. Gas is then driven out of the galactic disk in outflows when massive stars explode as supernovae and produce metal-enriched winds (e.g., Shen et al. 2012; Lehner et al. 2013; Ford et al. 2014; Muzahid et al. 2015). The velocities of the outflowing gas do not usually exceed the escape velocity of the galaxy (e.g., Tumlinson et al. 2011; Bouché et al. 2012; Stocke et al. 2013; Mathes et al. 2014; Bordoloi et al. 2014), thus the gas is recycled back onto the galaxy and could fuel further episodes of star formation (e.g., Oppenheimer et al. 2010; Ford et al. 2014; van de Voort 2017). This paints the

picture of the baryon cycle within the galaxy virial radius.

The O VI $\lambda\lambda1031, 1037$ absorption doublet is a common tracer of the CGM, particularly in the high-temperature regime of $T \sim 10^5$ K (e.g., Prochaska et al. 2011; Tumlinson et al. 2011; Stocke et al. 2013; Savage et al. 2014; Churchill et al. 2015; Johnson et al. 2015; Kacprzak et al. 2015; Werk et al. 2016). Oppenheimer et al. (2016) employed the EAGLE simulations to investigate the presence and role of different oxygen species in the CGM, assuming that O VI is collisionally ionized. They found that O VI is not the dominant oxygen species in the CGM, and that the column densities for O VI peak for L_* galaxies, while dropping for lower mass halos and group halos. This is thought to be due to the O VI ionization fraction strongly tracing the virial temperature of the galaxy, where the associated virial temperature for L_* galaxies provides the optimal conditions for the presence of O VI. For less massive galaxies, the virial temperature would be too cool for strong O VI presence, whereas the virial temperature would be too high for more group environments as a larger fraction of O VI is ionized out to higher ionization species. Nelson et al. (2018) found similar trends in the O VI column density with halo mass, but attributed them to black hole feedback (also see Oppenheimer et al. 2018).

Using a sample of quasar absorption-line spectra from *HST*/COS identified as part of the "Multiphase Galaxy Halos" Survey, Kacprzak et al. (2015) found that O VI has an azimuthal angle preference, where O VI tends to reside along

† masonng@mit.edu

the projected major axis ($0° \leq \Phi \leq 20°$) and/or along the projected minor axis ($60° \leq \Phi \leq 90°$). They also found a very weak dependence of the O VI absorption on the galaxy inclination, where the covering fraction of the O VI gas is roughly constant over all inclination angles except for $i > 70°$, as the high inclination minimizes the geometrical cross-section of gas flows. Moreover, the mean equivalent widths of O VI in lower inclination ($i < 45°$) galaxies and higher inclination ($i > 45°$) galaxies are consistent with each other.

Previous kinematics studies examined the absorber velocity dispersions of O VI with pixel-velocity two-point correlation functions (TPCFs) to characterize the absorber velocity dispersions for isolated galaxies (Nielsen et al. 2017). The authors found that there was no dependence of O VI kinematics on the inclination angle, azimuthal angle, and/or galaxy color, which indirectly suggests a lack of dependence on current star formation activity. They attribute this to O VI absorbers having ample time to mix and form a kinematically uniform halo surrounding the galaxies. This is consistent with Ford et al. (2014), who found that O VI in simulations likely traces gas that originates from ancient outflows. These results are in contrast to Mg II kinematics, which depends strongly on galaxy color, redshift, inclination, and azimuthal angle (Nielsen et al. 2015, 2016).

Pointon et al. (2017) examined O VI kinematics using TPCFs for galaxy group environments and found that the O VI absorption profiles for galaxy group environments are narrower compared to isolated galaxies. They posit that the virial temperature of the CGM in galaxy group environments (with more massive halos) is hot enough to ionize a larger fraction of O VI to higher order species to result in a lower ionization fraction compared to isolated galaxies, consistent with the findings of Oppenheimer et al. (2016). This suggests that halo mass needs to be considered when studying the absorber kinematics of O VI.

Focusing on O VI absorber–galaxy kinematics, Tumlinson et al. (2011) found that O VI absorber–galaxy velocities rarely exceed the host galaxy escape velocity, indicating that the gas is bound. Mathes et al. (2014) found similar results, but noted that the fraction of gas that exceeds host galaxy escape velocities decreases with increasing halo mass. The authors suggested that wind recycling is increasingly important as the halo mass increases, consistent with simulations (Oppenheimer et al. 2010). Most recently, Kacprzak et al. (2019) related O VI absorber kinematics to host galaxy rotation curves. They found that along the projected galaxy major axis, where accretion is expected, O VI does not correlate with galaxy rotation kinematics like Mg II (e.g., Steidel et al. 2002; Kacprzak et al. 2010, 2011; Ho et al. 2017). For gas observed along the projected galaxy minor axis, O VI absorbers best match models of decelerating outflows. Combined with simulations, the authors suggest that O VI is not an ideal probe of gas accretion or outflows, but rather traces the virial temperature of the host halo.

The work presented here will address both the halo mass dependence of O VI absorber kinematics, and how O VI gas flows relative to the host galaxies by examining the absorber–galaxy kinematics using a subset of O VI absorbers from the "Multiphase Galaxy Halos" Survey. We employ two TPCF methods: (1) absorber kinematics, which is the approach employed by Nielsen et al. (2017), and (2) absorber–galaxy kinematics. In constructing the TPCFs for absorber–galaxy kinematics (method 2), we apply the velocity offset between the absorber redshift and the galaxy redshift. We also normalize

the absorber–galaxy velocities with respect to the circular velocity at the observed impact parameter, $V_c(D)$, to take into consideration the range of halo masses in the sample (similar to the normalization done in Nielsen et al. 2016). Average absorption profiles are presented to complement the TPCFs by providing information about the optical depth.

In Section 2, we present the sample and elaborate on how the kinematics are quantified, namely with the TPCFs and average absorption profiles. In Section 3, we present the mass dependence of absorber kinematics, comparing our sample to the group environment sample published in Pointon et al. (2017) and the simulated aperture column densities presented by Oppenheimer et al. (2016). Section 4 presents new absorber–galaxy kinematics for various subsamples segregated by galaxy redshift, z_{gal}, inclination, i, azimuthal angle, Φ, and halo mass, $\log(M_h/M_\odot)$. In Section 5, we discuss the halo mass dependence of O VI absorber kinematics and non-virialized motions in the form of outflows. Finally, we conclude in Section 6. Throughout we assume a ΛCDM cosmology ($H_0 = 70\,\mathrm{km\,s^{-1}\,Mpc^{-1}}, \Omega_M = 0.3, \Omega_\Lambda = 0.7$).

2. SAMPLE AND DATA ANALYSIS

The sample of O VI absorber–galaxy pairs used in this work is a subset of the "Multiphase Galaxy Halos" Survey (Kacprzak et al. 2015, 2019; Muzahid et al. 2015, 2016; Nielsen et al. 2017; Pointon et al. 2017, 2019). The associated galaxy spectroscopic redshifts, z_{gal}, spanning $0.1241 \leq z_{gal} \leq 0.6610$ (median $\langle z_{gal} \rangle = 0.2443$), are accurate to within $\sigma_z \leq 0.0001$, which is $\sim 30\,\mathrm{km\,s^{-1}}$ in velocity space (e.g., Kacprzak et al. 2019). The absorber–galaxy pairs are also within an on-the-sky projected distance (impact parameter) of $D \approx 200$ kpc (21.1 kpc$< D <$ 276.3 kpc, median $\langle D \rangle$ = 93.2 kpc). All of the galaxies are isolated, that is, there were no identified neighboring galaxies within a projected distance of 200 kpc from the line-of-sight of the quasar, and within a line-of-sight velocity separation of 500 km s^{-1}. Absorption systems with line-of-sight velocities larger than ± 500 km s^{-1} away from their identified host galaxies are assumed not to be associated with the host galaxy.

For our O VI absorber kinematics analysis (Section 3), we also include a sample of six galaxy group environments from Pointon et al. (2017) for comparison. See Pointon et al. (2017) for further details. We include this sample to cover a large range in halo masses to investigate the O VI column density dependence on halo mass found in the EAGLE simulations (Oppenheimer et al. 2016).

2.1. *Galaxy Properties*

We have selected 31 absorber–galaxy pairs from the "Multiphase Galaxy Halos" Survey that are suitable for this study. Each galaxy in the sample was imaged with ACS, WFC3, or WFPC2 on the *Hubble Space Telescope (HST)*. GIM2D (Simard et al. 2002) was then used to model the morphological properties of the galaxies; the details of the modeling are elaborated upon in Kacprzak et al. (2015). Following Nielsen et al. (2017), we define galaxies having inclination angles of $0° \leq i < 51°$ as face-on, and galaxies with $51° \leq i \leq 90°$ as edge-on. We also define azimuthal angles of $0° \leq \Phi < 45°$ as a quasar sightline aligned with the projected major axis of the galaxy, and azimuthal angles of $45° \leq \Phi \leq 90°$ as a quasar sightline aligned with the projected minor axis of the galaxy.

To measure accurate redshifts, galaxy spectra were obtained for a majority of our sample (24/31) using the Keck Echellette

Table 1
O VI Absorber–Galaxy Properties

(1) Field	(2) $z_{\rm gal}$	(3) Ref [a]	(4) $z_{\rm abs}$	(5) $W_{\rm r}(1031)$ (Å)	(6) Φ (deg)	(7) i (deg)	(8) $\log(M_{\rm h}/M_\odot)$	(9) $V_{\rm c}(D)$ (km s^{-1})	(10) D (kpc)	(11) $R_{\rm vir}$ (kpc)
J012528$-$000555	0.3985252	1	0.399090	0.817	$73.4^{+4.6}_{-4.7}$	$63.2^{+1.7}_{-2.6}$	$12.51^{+0.16}_{-0.15}$	$242.9^{+68.8}_{-53.6}$	163.0 ± 0.1	$285.4^{+37.3}_{-32.0}$
J035128$-$142908	0.3569918	1	0.356825	0.396	$4.9^{+33.0}_{-40.2}$	$28.5^{+19.8}_{-12.5}$	$12.00^{+0.29}_{-0.19}$	$174.8^{+90.9}_{-50.6}$	72.3 ± 0.4	$190.8^{+47.9}_{-25.9}$
J040748$-$121136	0.3422	2	0.342042	0.056	$48.1^{+1.0}_{-0.9}$	$85.0^{+0.1}_{-0.4}$	$11.62^{+0.42}_{-0.21}$	$107.5^{+83.8}_{-36.9}$	172.0 ± 0.1	$142.5^{+53.9}_{-21.6}$
J040748$-$121136	0.4951635	3	0.495101	0.229	$21.0^{+5.3}_{-3.7}$	$67.2^{+7.6}_{-7.5}$	$11.41^{+0.45}_{-0.21}$	$97.5^{+82.6}_{-33.7}$	107.6 ± 0.4	$124.4^{+51.6}_{-18.2}$
J045608$-$215909	0.3815113	1	0.381514	0.219	$63.8^{+4.3}_{-2.7}$	$57.1^{+19.9}_{-2.4}$	$12.00^{+0.29}_{-0.19}$	$167.7^{+86.8}_{-48.4}$	103.4 ± 0.3	$192.4^{+48.0}_{-26.0}$
J091440$+$282330	0.2443121	1	0.244098	0.333	$18.2^{+1.1}_{-1.0}$	$39.0^{+0.4}_{-0.2}$	$11.88^{+0.33}_{-0.20}$	$153.2^{+91.5}_{-46.9}$	105.9 ± 0.1	$170.7^{+49.4}_{-23.9}$
J094331$+$053131	0.3530520	1	0.353286	0.220	$8.2^{+3.0}_{-5.0}$	$44.4^{+1.1}_{-1.2}$	$11.66^{+0.41}_{-0.21}$	$125.9^{+95.4}_{-42.6}$	96.5 ± 0.3	$146.8^{+54.1}_{-22.0}$
J094331$+$053131	0.5484936	1	0.548769	0.275	$67.2^{+0.9}_{-1.0}$	$58.8^{+0.6}_{-1.1}$	$11.96^{+0.26}_{-0.18}$	$150.3^{+70.2}_{-41.3}$	150.9 ± 0.6	$190.9^{+42.9}_{-24.9}$
J095000$+$483129	0.2118657	1	0.211757	0.211	$16.6^{+0.1}_{-0.1}$	$47.7^{+0.1}_{-0.1}$	$12.37^{+0.18}_{-0.16}$	$237.0^{+74.7}_{-55.3}$	93.6 ± 0.2	$246.9^{+36.1}_{-29.0}$
J100402$+$285535	0.1380	4	0.137724	0.117	$12.4^{+2.4}_{-2.9}$	$79.1^{+2.2}_{-2.1}$	$10.87^{+0.63}_{-0.22}$	$69.9^{+89.3}_{-27.6}$	56.7 ± 0.2	$76.3^{+47.3}_{-11.7}$
J100902$+$071343	0.2278553	1	0.227851	0.576	$89.6^{+1.3}_{-1.3}$	$66.3^{+0.6}_{-0.9}$	$11.76^{+0.37}_{-0.21}$	$149.0^{+101.2}_{-48.2}$	64.0 ± 0.8	$154.5^{+50.9}_{-22.5}$
J104116$+$061016	0.4421726	1	0.441630	0.368	$4.3^{+0.9}_{-1.0}$	$49.8^{+7.4}_{-5.2}$	$11.99^{+0.26}_{-0.18}$	$173.8^{+79.1}_{-47.1}$	56.2 ± 0.3	$193.1^{+42.2}_{-24.9}$
J111908$+$211918	0.1383	5	0.138521	0.074	$34.4^{+0.4}_{-0.4}$	$26.4^{+0.8}_{-0.4}$	$12.24^{+0.21}_{-0.17}$	$204.3^{+76.5}_{-51.4}$	138.0 ± 0.2	$219.0^{+38.8}_{-27.1}$
J113327$+$032719	0.1545985	3	0.153979	0.252	$56.1^{+1.7}_{-1.3}$	$23.5^{+0.4}_{-0.2}$	$11.64^{+0.41}_{-0.21}$	$139.8^{+107.1}_{-47.5}$	55.6 ± 0.1	$138.7^{+51.6}_{-20.9}$
J113910$-$135043	0.2041940	1	0.204297	0.231	$5.8^{+0.4}_{-0.5}$	$83.4^{+0.4}_{-0.5}$	$11.69^{+0.40}_{-0.21}$	$133.0^{+98.0}_{-44.3}$	93.2 ± 0.3	$146.2^{+52.4}_{-21.6}$
J113910$-$135043	0.2122591	1	0.212237	0.137	$80.4^{+0.4}_{-0.5}$	$85.0^{+5.0}_{-5.0}$	$11.73^{+0.39}_{-0.21}$	$119.2^{+84.4}_{-39.2}$	174.8 ± 0.1	$150.3^{+51.7}_{-22.0}$
J113910$-$135043	0.2197242	3	0.219820	0.021	$44.9^{+8.9}_{-8.1}$	$85.0^{+5.0}_{-8.5}$	$11.04^{+0.60}_{-0.21}$	$66.8^{+80.5}_{-25.8}$	122.0 ± 0.2	$88.7^{+52.0}_{-13.5}$
J113910$-$135043	0.3192551	1	0.319167	0.255	$39.1^{+1.9}_{-1.7}$	$83.4^{+1.4}_{-1.1}$	$11.86^{+0.34}_{-0.20}$	$157.0^{+96.1}_{-48.5}$	73.3 ± 0.4	$170.4^{+50.7}_{-23.9}$
J121920$+$063838	0.1241	5	0.124103	0.424	$67.2^{+39.8}_{-91.4}$	$22.0^{+18.7}_{-21.8}$	$11.87^{+0.34}_{-0.20}$	$156.8^{+95.6}_{-48.4}$	93.4 ± 5.3	$163.1^{+48.2}_{-22.9}$
J123304$-$003134	0.3187570	3	0.318609	0.439	$17.0^{+2.0}_{-2.3}$	$38.7^{+1.6}_{-1.8}$	$11.91^{+0.32}_{-0.20}$	$159.2^{+92.5}_{-48.3}$	88.9 ± 0.2	$176.5^{+49.7}_{-24.7}$
J124154$+$572107	0.2052671	1	0.205538	0.519	$77.6^{+0.3}_{-0.4}$	$56.4^{+0.3}_{-0.5}$	$11.64^{+0.41}_{-0.21}$	$145.0^{+114.4}_{-49.3}$	21.1 ± 0.1	$140.2^{+52.3}_{-21.1}$
J124154$+$572107	0.2179045	3	0.218043	0.366	$63.0^{+1.8}_{-2.1}$	$17.4^{+1.4}_{-1.6}$	$11.62^{+0.42}_{-0.21}$	$124.0^{+96.7}_{-42.5}$	94.6 ± 0.2	$138.7^{+52.4}_{-21.0}$
J124410$+$172104	0.5504	4	0.550622	0.447	$20.1^{+16.7}_{-19.1}$	$31.7^{+16.2}_{-4.8}$	$11.82^{+0.31}_{-0.19}$	$144.4^{+79.0}_{-42.3}$	21.2 ± 0.3	$171.2^{+45.5}_{-23.1}$
J131956$+$272808	0.6610	6	0.660670	0.311	$86.6^{+1.5}_{-1.2}$	$65.8^{+1.2}_{-1.2}$	$12.15^{+0.19}_{-0.15}$	$183.6^{+59.8}_{-41.6}$	103.9 ± 0.5	$223.9^{+34.7}_{-24.9}$
J132222$+$464546	0.2144314	1	0.214320	0.354	$13.9^{+0.2}_{-0.2}$	$57.9^{+0.1}_{-0.2}$	$12.13^{+0.25}_{-0.18}$	$204.0^{+90.8}_{-54.7}$	38.6 ± 0.2	$204.6^{+43.8}_{-26.1}$
J134251$-$005345	0.2270416	1	0.227196	0.373	$13.2^{+0.5}_{-0.4}$	$0.1^{+0.6}_{-0.1}$	$12.39^{+0.17}_{-0.16}$	$239.3^{+73.7}_{-55.2}$	35.3 ± 0.2	$251.7^{+35.9}_{-29.3}$
J155504$+$362847	0.1892007	1	0.189033	0.385	$47.0^{+0.3}_{-0.8}$	$51.8^{+0.7}_{-0.7}$	$12.07^{+0.27}_{-0.18}$	$196.3^{+93.8}_{-54.2}$	33.4 ± 0.1	$193.7^{+44.6}_{-25.2}$
J213135$-$120704	0.4302	7	0.430164	0.385	$14.9^{+6.0}_{-4.9}$	$48.3^{+3.5}_{-3.7}$	$12.04^{+0.25}_{-0.18}$	$181.3^{+79.0}_{-48.1}$	48.4 ± 0.2	$199.7^{+41.8}_{-25.3}$
J225357$+$160853	0.1537175	8	0.153821	0.263	$59.6^{+0.9}_{-1.8}$	$33.3^{+2.7}_{-2.0}$	$11.55^{+0.45}_{-0.21}$	$137.8^{+115.4}_{-48.1}$	31.8 ± 0.2	$129.5^{+52.7}_{-19.6}$
J225357$+$160853	0.3527870	1	0.352708	0.381	$88.7^{+4.6}_{-4.8}$	$36.7^{+6.9}_{-4.6}$	$11.93^{+0.32}_{-0.20}$	$138.1^{+78.4}_{-41.6}$	203.2 ± 0.5	$180.3^{+49.5}_{-25.2}$
J225357$+$160853	0.3900125	8	0.390705	0.173	$24.2^{+1.2}_{-1.2}$	$76.1^{+1.1}_{-1.2}$	$12.16^{+0.24}_{-0.18}$	$160.4^{+69.0}_{-42.5}$	276.3 ± 0.2	$217.2^{+44.9}_{-27.5}$

[a] Galaxy redshift references: (1) Kacprzak et al. (2019), (2) Muzahid et al. (2015), (3) Johnson et al. (2013), (4) Pointon et al. (2019), (5) Chen et al. (2001), (6) Prochaska et al. (2011), (7) Kacprzak et al. (2012), (8) Guillemin & Bergeron (1997), and (9) this work.

Spectrograph and Imager, ESI (Sheinis et al. 2002). Details of the observations and data reduction, and most of the new redshifts are presented in Kacprzak et al. (2019). Several additional redshifts determined with this method are presented in Pointon et al. (2019) and here. The ESI spectra have a resolution of 22 km s^{-1} pixel^{-1} (FWHM $\sim$ 90 km/s) when binned by two in the spectral direction and have a wavelength coverage of 4000 to 10000 Å, which allows for detection of multiple emission lines such as the [O II] doublet, Hβ, [O III] doublet, Hα, and [N II] doublet. Galaxy spectra are both vacuum and heliocentric velocity-corrected to provide a direct comparison with the absorption line spectra. The Gaussian fitting algorithm FITTER (Churchill et al. 2000) was used to compute best-fit emission-line centroids and widths to derive galaxy redshifts. Galaxy redshifts obtained with ESI have accuracies ranging from $3 - 20$ km s^{-1}. The remainder of the galaxy red-

shifts were obtained from previous studies, and are tabulated in Table 1 (Guillemin & Bergeron 1997; Chen et al. 2001; Prochaska et al. 2011; Kacprzak et al. 2012; Johnson et al. 2013).

Since previous work has suggested that halo mass is key to governing the presence or absence of O VI absorbing gas (e.g., Oppenheimer et al. 2016; Pointon et al. 2017), we calculate halo masses, circular velocities, and virial radii for each of the galaxies in our sample to investigate this mass dependence for gas kinematics. We follow the halo abundance matching method described in Appendix A of Churchill et al. (2013) and summarize it here (also see Trujillo-Gomez et al. 2011). Halo abundance matching makes the assumption that the number density of galaxies with a given observed galaxy property (in this case, the COMBO-17 $r-$band luminosity functions from Wolf et al. 2003) is mapped to the dis-

tribution function of simulated galaxies with a given property (the maximum circular velocity or dark matter halo mass from the Bolshoi *N*-body cosmological simulation dark matter halo catalogs; Klypin et al. 2011). For each galaxy in our sample, the *r*−band absolute Vega magnitude, $M_r - 5\log(h)$, was calculated and used in the corresponding redshift curves from Figure 9(b) of Churchill et al. (2013) to calculate halo masses, $\log(M_h/M_\odot)$. From the halo masses, we calculate the virial radii according to Bryan & Norman (1998). Circular velocities, $V_c(D)$, were calculated at the impact parameter of absorption using Equations 5 of Navarro et al. (1996) and B2 of Churchill et al. (2013). In the sample, the halo masses span $10.87 \leq \log(M_h/M_\odot) \leq 12.51$ (median $\langle \log(M_h/M_\odot) \rangle = 11.88$); the circular velocities span 66.8 km s^{-1} $\leq V_c(D) \leq 242.9$ km s^{-1} (median $\langle V_c(D) \rangle = 150.3$ km s^{-1}).

In Table 1, we list the absorber–galaxy pairs used in this work, the corresponding galaxy redshifts, z_{gal}, O VI absorber redshifts, z_{abs}, rest-frame equivalent widths, $W_r(1031)$, azimuthal angle, Φ, galaxy inclination, i, halo mass, $\log(M_h/M_\odot)$, circular velocity at the observed impact parameter, $V_c(D)$, impact parameter, D, and the virial radius, R_{vir}. The subsample cuts, number of galaxies, median halo masses, and median redshifts for each subsample are listed in Table 2.

In the sample, rank correlation tests yield no statistically significant correlations between the galaxy redshift, azimuthal angle, inclination, and halo mass. A one-dimensional Kolmogorov-Smirnov (KS) test was also carried out on the galaxy orientation measurements to test whether the sample is unbiased. We find that the azimuthal angles of the galaxies are consistent with that of unbiased samples at the 0.6σ level; the inclination angles of the galaxies are also consistent with that of unbiased samples at the 2.3σ level.

2.2. *Quasar Spectra*

The details of the quasar spectra are found in Kacprzak et al. (2015) and Nielsen et al. (2017), but we summarize them here. Each of the 23 quasars has a medium resolution ($R \sim 20,000$, FWHM ~ 18 km s^{-1}) spectrum from *HST*/COS. Voigt profiles were fitted to each of the O VI $\lambda\lambda 1031, 1037$ doublet absorption lines with VPFIT (Carswell & Webb 2014), and the zero-points of velocity (i.e., z_{abs}) were defined as the velocity where 50% of the modeled absorption resides on each side in the optical depth distribution for the O VI $\lambda 1031$ line (Nielsen et al. 2017). The velocity bounds of the absorption were defined to be where modeled absorption deviates from the continuum (value of 1) by 1% (to 0.99).

2.3. *Pixel-Velocity Two-Point Correlation Function*

The TPCF method has previously been used to analyze the absorber velocity dispersions of Mg II and O VI absorbers surrounding galaxies (Nielsen et al. 2015, 2016, 2017, 2018; Pointon et al. 2017). In the first part of this work, we investigate the mass dependence of the velocity dispersions of the absorbers ("absorber kinematics"). For the rest of this work, we shift the velocities relative to the galaxy systemic velocity to investigate the motion of the surrounding gas relative to the galaxy ("absorber–galaxy kinematics").

2.3.1. *Absorber Kinematics*

The details of the absorber TPCF construction are expounded in Nielsen et al. (2016), but we briefly summarize the method here. The velocities of all the pixels within the velocity bounds in which O VI absorption is formally detected

are first extracted for a desired subsample (e.g., all edge-on galaxies) and combined into a single array. Statistically, for a given subsample, this step makes the equivalency between a single quasar absorption sightline around multiple galaxies, and a single galaxy with multiple sightlines. We then calculate the absolute value of the velocity separations between every pair of pixel velocities in the subsample, Δv_{pix}. These velocity separations are binned into 20 km s^{-1} bins to account for the resolution of COS and the number of counts in each bin is normalized by the total number of velocity separation pairs in the subsample. This yields a probability distribution function of the velocity dispersion, the absorber TPCF.

The uncertainties on the TPCFs were determined by a bootstrap analysis with 100 bootstrap realizations where absorber–galaxy pairs were randomly drawn with replacement. These are 1σ uncertainties from the mean of the bootstrap realizations. To characterize the TPCFs, we use the quantities $\Delta v(50)$ and $\Delta v(90)$. These represent the velocity separations within which 50% and 90% of the area under the TPCF is located. Following Nielsen et al. (2015), we employ two-sample χ^2 tests to examine and quantify statistical differences between the TPCFs of different galaxy-absorber subsamples. We report the reduced χ^2, i.e., χ^2_ν, where ν is the number of degrees of freedom.

2.3.2. *Absorber–Galaxy Kinematics*

The TPCFs described in the previous section were modified to account for the velocity of the gas relative to the host galaxy. After the pixel velocities are extracted from a subsample, they are shifted with respect to the host galaxy,

$$v_{pix-gal} = \left| v_{pix} + c \frac{z_{abs} - z_{gal}}{1 + z_{gal}} \right|. \quad (1)$$

We take the absolute value of this shifted velocity to quantify the velocity dispersion of the absorbing gas with respect to the galaxy systemic velocity, without considering its direction. We also do not know whether the gas is physically located in front of or behind the host galaxy, so we cannot determine if the gas is infalling or outflowing relative to the galaxy, hence the velocity sign is not important. Thus, in this work, the absorber–galaxy TPCF is defined to be a statistical measure of the velocity dispersion of the absorbers whose velocities are shifted with respect to the galaxy systemic velocity.

Since our sample of galaxies spans a range of halo masses, we account for the galaxy halo mass by normalizing the shifted velocities by the circular velocity at the observed impact parameter of the host galaxy, $V_c(D)$. We now work with the circular velocity-normalized pixel–galaxy velocities, $v_{pix-gal}/V_c(D)$. Once these values are obtained, the normalized velocities for a given subsample are combined and are subtracted between every possible pair of pixels. Thus we obtain normalized pixel–galaxy velocity separations, $\Delta(v_{pix-gal}/V_c(D))$.

For the absorber–galaxy TPCF, we use a bin size of $\Delta(v_{pix-gal}/V_c(D)) = 0.2$, which is determined by dividing the maximum uncertainty of the systemic galaxy redshift, $\Delta z_{gal} = 0.0001$, corresponding to $\sim 30/(1 + \langle z_{gal} \rangle)$ km s^{-1} in the galaxy rest frame, by the average $V_c(D)$ in the sample, 156 km s^{-1}.

2.4. *Average Absorption Profiles*

Table 2
TPCF $\Delta v(50)$ and $\Delta v(90)$ measurements

Subsample	# galaxies	Cut 1	Cut 2	$\langle \log(M_{\rm h}/M_\odot) \rangle$	$\langle z_{\rm gal} \rangle$	$\Delta v(50)$	$\Delta v(90)$
		Figure 1: Absorber Kinematics				$v = v_{\rm pix}$ (km s^{-1})	
Lower Mass	10	$\log(M_{\rm h}/M_\odot) < 11.7$	...	11.62 ± 0.09	0.21 ± 0.03	80^{+5}_{-8}	188^{+11}_{-19}
Higher Mass	21	$\log(M_{\rm h}/M_\odot) \geq 11.7$	...	12.00 ± 0.04	0.32 ± 0.03	108^{+6}_{-9}	255^{+14}_{-22}
Group [a]	6	...	...	...	0.19 ± 0.05	64^{+9}_{-7}	153^{+21}_{-18}
		Figure 3: Absorber–Galaxy Kinematics				$v = v_{\rm pix-gal}/V_{\rm c}(D)$	
Lower Mass	15	$\log(M_{\rm h}/M_\odot) < 11.88$	...	11.64 ± 0.04	0.22 ± 0.03	$0.45^{+0.03}_{-0.03}$	$1.12^{+0.08}_{-0.09}$
Higher Mass	16	$\log(M_{\rm h}/M_\odot) \geq 11.88$	...	12.06 ± 0.07	0.34 ± 0.05	$0.34^{+0.02}_{-0.02}$	$0.87^{+0.06}_{-0.07}$
		Figure 4: Absorber–Galaxy Kinematics				$v = v_{\rm pix-gal}/V_{\rm c}(D)$	
Lower-z	15	$z_{\rm gal} < 0.244$	...	11.73 ± 0.18	0.205 ± 0.016	$0.40^{+0.04}_{-0.04}$	$1.11^{+0.11}_{-0.12}$
Higher-z	16	$z_{\rm gal} \geq 0.244$	...	11.95 ± 0.05	0.39 ± 0.03	$0.37^{+0.02}_{-0.02}$	$0.92^{+0.04}_{-0.05}$
		Not Plotted: Absorber–Galaxy Kinematics				$v = v_{\rm pix-gal}/V_{\rm c}(D)$	
Face-on	15	$i < 51°$	...	11.82 ± 0.14	0.32 ± 0.09	$0.40^{+0.03}_{-0.04}$	$1.03^{+0.09}_{-0.12}$
Edge-on	16	$i \geq 51°$	...	11.91 ± 0.08	0.24 ± 0.05	$0.38^{+0.02}_{-0.03}$	$0.96^{+0.07}_{-0.08}$
Major Axis	17	$\Phi < 45°$	...	11.76 ± 0.16	0.23 ± 0.06	$0.35^{+0.02}_{-0.03}$	$0.90^{+0.06}_{-0.09}$
Minor Axis	14	$\Phi \geq 45°$	...	11.92 ± 0.06	0.33 ± 0.05	$0.42^{+0.04}_{-0.03}$	$1.07^{+0.10}_{-0.10}$
		Figure 5: Absorber–Galaxy Kinematics				$v = v_{\rm pix-gal}/V_{\rm c}(D)$	
Major Axis + Face-on	10	$\Phi < 45°$	$i < 51°$	12.00 ± 0.12	0.32 ± 0.05	$0.35^{+0.02}_{-0.03}$	$0.87^{+0.06}_{-0.09}$
Major Axis + Edge-on	7	$\Phi < 45°$	$i \geq 51°$	11.69 ± 0.32	0.26 ± 0.07	$0.38^{+0.06}_{-0.05}$	$0.97^{+0.20}_{-0.17}$
Minor Axis + Face-on	5	$\Phi \geq 45°$	$i < 51°$	11.64 ± 0.17	0.18 ± 0.05	$0.51^{+0.04}_{-0.06}$	$1.24^{+0.10}_{-0.16}$
Minor Axis + Edge-on	9	$\Phi \geq 45°$	$i \geq 51°$	11.96 ± 0.13	0.32 ± 0.08	$0.38^{+0.02}_{-0.03}$	$0.96^{+0.07}_{-0.08}$
		Figure 6: Absorber–Galaxy Kinematics				$v = v_{\rm pix-gal}/V_{\rm c}(D)$	
Major Axis + Lower Mass	7	$\Phi < 45°$	$\log(M_{\rm h}/M_\odot) < 11.88$	11.66 ± 0.15	0.31 ± 0.09	$0.40^{+0.04}_{-0.04}$	$1.02^{+0.15}_{-0.16}$
Major Axis + Higher Mass	10	$\Phi < 45°$	$\log(M_{\rm h}/M_\odot) \geq 11.88$	12.09 ± 0.09	0.29 ± 0.06	$0.33^{+0.02}_{-0.03}$	$0.83^{+0.06}_{-0.09}$
Minor Axis + Lower Mass	8	$\Phi \geq 45°$	$\log(M_{\rm h}/M_\odot) < 11.88$	11.64 ± 0.05	0.20 ± 0.02	$0.48^{+0.03}_{-0.04}$	$1.17^{+0.07}_{-0.11}$
Minor Axis + Higher Mass	6	$\Phi \geq 45°$	$\log(M_{\rm h}/M_\odot) \geq 11.88$	12.04 ± 0.14	0.41 ± 0.07	$0.37^{+0.03}_{-0.03}$	$0.92^{+0.10}_{-0.11}$
Face-on + Lower Mass	6	$i < 51°$	$\log(M_{\rm h}/M_\odot) < 11.88$	11.65 ± 0.09	0.22 ± 0.08	$0.51^{+0.03}_{-0.05}$	$1.23^{+0.08}_{-0.14}$
Face-on + Higher Mass	9	$i < 51°$	$\log(M_{\rm h}/M_\odot) \geq 11.88$	12.00 ± 0.15	0.30 ± 0.06	$0.33^{+0.03}_{-0.02}$	$0.81^{+0.08}_{-0.06}$
Edge-on + Lower Mass	9	$i \geq 51°$	$\log(M_{\rm h}/M_\odot) < 11.88$	11.64 ± 0.10	0.23 ± 0.04	$0.40^{+0.03}_{-0.03}$	$0.99^{+0.11}_{-0.10}$
Edge-on + Higher Mass	7	$i \geq 51°$	$\log(M_{\rm h}/M_\odot) \geq 11.88$	12.13 ± 0.08	0.39 ± 0.08	$0.37^{+0.03}_{-0.03}$	$0.93^{+0.09}_{-0.10}$

[a] Data from Pointon et al. (2017).

We complement the TPCFs with the average absorption profiles for a given subsample. The average profiles provide supplementary information about the optical depth distribution and indicate how much gas there is at a given velocity.

The average absorption profiles were constructed by first extracting the pixel velocities. For absorber kinematics, we do not modify these velocities. For absorber–galaxy kinematics, we shift the velocities relative to the galaxy systemic velocity and normalize them with respect to the galaxy's circular velocity, $V_{\rm c}(D)$. The associated flux values, obtained using model absorption profiles to the data to remove any contami-

nation due to noise and blends on the flux, are also extracted. Next, for any given profile, the positive pixel velocities and negative pixel velocities are separated into two arrays. We take the absolute value of the negative velocities because we do not know where the gas is located relative to the galaxy other than the projected distance, thus the sign on the velocities bears little meaning. Then for both the velocity and flux arrays we run a linear interpolation routine onto a standardized velocity grid to place all absorbers on the same velocity or absorber–galaxy normalized velocity scale. This is repeated for all the absorber–galaxy pairs in the subsample.
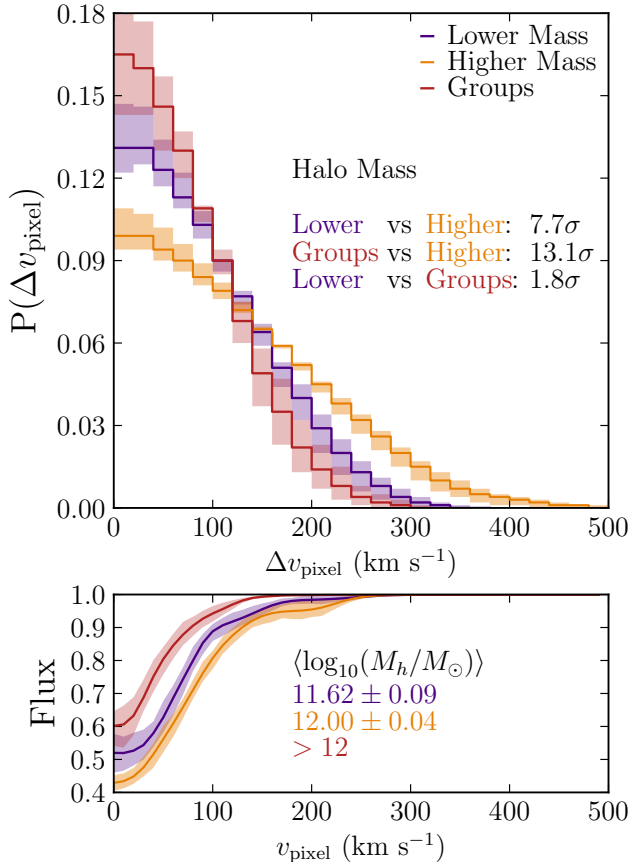
Figure 1. (Top) Absorber TPCFs for lower mass (purple), higher mass (orange), and group (red) galaxies. The higher mass galaxies have significantly larger velocity dispersions compared with the lower mass galaxies (7.7σ) and group galaxies (13.1σ). Group galaxies from Pointon et al. (2017) have similar velocity dispersions to lower mass galaxies. (Bottom) Average absorption profiles corresponding to lower mass galaxies, higher mass galaxies, and group galaxies. Group galaxies have lower optical depth at all pixel velocities compared with lower and higher mass galaxies. 1σ uncertainties for both the TPCFs and average absorption spectra were calculated with a bootstrap analysis with 100 bootstrap realizations.

3. ABSORBER KINEMATICS

We first investigate the dependence of O VI absorber kinematics on halo mass in Figure 1. The isolated galaxy sample is sliced by $\log(M_{\rm h}/M_\odot) = 11.7$, which was motivated by Oppenheimer et al. (2016) who used it to define sub-L^* and L^* galaxies, which we call "lower mass" and "higher mass" galaxies here, respectively. We also show the group galaxy sample from Pointon et al. (2017) to study a more complete mass range for better comparison with the simulations. The group sample was defined by the number of galaxies and not mass since halo masses derived by halo abundance matching may not be representative of the entire group halo. Oppenheimer et al. (2016) defined group halos as those with
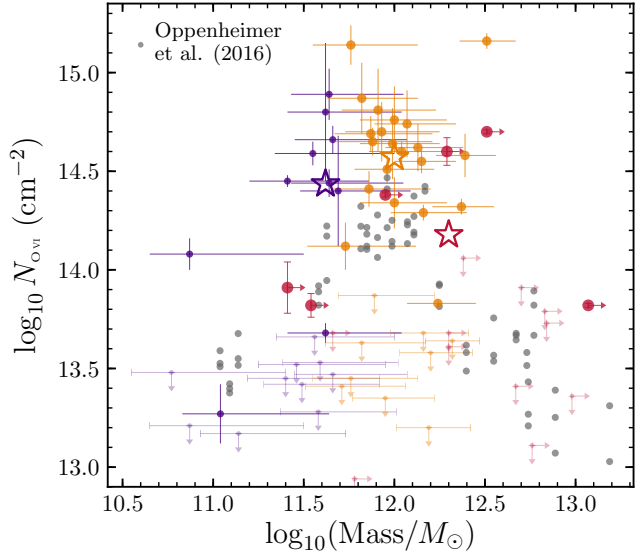

Figure 2. Column densities and masses for observational and simulation data. Lower mass galaxies are represented by purple points, higher mass are orange, and group galaxies are red. Because the group galaxy masses are difficult to estimate, their masses are plotted as lower limits. Upper limits on absorption are plotted as small points with downward arrows. Stars indicate the column densities obtained from the average absorption profiles presented in Figure 1, where the halo mass is determined by the median halo mass for the lower and higher mass subsamples. Gray points are the aperture column densities within 150 kpc and M_{200} masses from Oppenheimer et al. (2016). Our data follow the trend of increasing column densities toward a maximum for L^* galaxies, and decreasing toward the highest masses.

$\log(M_{\rm h}/M_\odot) \geq 12.3$, but here we assume a more conservative mass of $\log(M_{\rm h}/M_\odot) > 12$ in the TPCF studies. If we calculate a mass for each group member galaxy with halo abundance matching and sum these values, we can obtain a lower limit on the group mass. We only use these values in Figure 2. While these group masses span all three mass subsamples, the group environments may have different absorption characteristics due to interaction effects (Alonso et al. 2012; Fernández et al. 2015; Pointon et al. 2017) so we consider these to be a separate sample.

In Figure 1 higher mass galaxies have significantly larger velocity dispersions than lower mass galaxies (7.7σ) and group galaxies (13.1σ), while group galaxies have similar velocity dispersions to lower mass galaxies (1.8σ). From Table 2, the $\Delta v(50)$ and $\Delta v(90)$ measurements for the lower mass galaxies (80^{+5}_{-8} km s^{-1} and 188^{+11}_{-19} km s^{-1}, respectively) and group galaxies (64^{+9}_{-7} km s^{-1} and 153^{+21}_{-18} km s^{-1}, respectively) are all consistent within uncertainties. However, higher mass galaxies have significantly larger $\Delta v(50)$ (108^{+6}_{-9} km s^{-1}) and $\Delta v(90)$ (255^{+14}_{-22} km s^{-1}) values than for either lower mass galaxies or group galaxies.

This effect is also observed in the average absorption profiles plotted in the bottom panel of Figure 1. Higher mass galaxies have the most optical depth at all line of sight velocities compared to lower mass and group galaxies, while group galaxies have the least optical depth at all line of sight velocities. We determined column densities for each average absorption profile by mirroring the plotted profile over $v_{\rm pixel} = 0$ km s^{-1} (the resulting profile is symmetric) and modeling the profiles with VPFIT as was done for the actual O VI profiles. We find column densities of $\log N_{\rm OVI} = 14.570$ for higher mass galaxies, $\log N_{\rm OVI} = 14.436$ for lower mass galax-

ies, and $\log N_{\rm O VI} = 14.178$ for group galaxies. As expected, the higher mass galaxies have the largest column densities and group galaxies have the smallest.

Because we are probing different mass galaxies with our quasar sightlines, we may be biased toward probing the inner regions of more massive galaxies. This is important because O VI equivalent widths and column densities decrease with increasing impact parameter (e.g., Tumlinson et al. 2011; Kacprzak et al. 2015). The median impact parameter normalized by the virial radius, $D/R_{\rm vir}$, for lower mass galaxies is 0.67, for higher mass galaxies is 0.46, and for group galaxies is 0.47. However, a KS test comparing the $D/R_{\rm vir}$ distributions suggest that the lower and higher mass galaxy subsamples were drawn from the same population (2.1σ). Comparing to the group galaxy sample, we find significances of 0.0σ for group galaxies versus higher mass galaxies and 0.6σ for group galaxies versus lower mass galaxies. The $D/R_{\rm vir}$ ranges for all three subsamples are also consistent. Thus differences in $D/R_{\rm vir}$ between the subsamples does not appear to strongly influence our results.

To better compare the kinematics results with the Oppenheimer et al. (2016) simulations, we plot our data and the simulation data on the column density–mass plane in Figure 2. The observational data plotted are line-of-sight column densities and halo masses from halo abundance matching. Halo masses of group galaxies are measured using the same method, but the individual galaxy masses are summed for each group to give a lower limit. Points are colored and sized by the three halo mass bins from Figure 1. The simulation data are plotted as gray points and represent aperture column densities within $D = 150$ kpc as a function of $\log(M_{200}/M_\odot)$. The column densities measured from the average absorption profiles in the previous paragraph are plotted as stars for each mass subsample. Our data generally follow the simulated trend that column densities increase with increasing mass up to $\log(M_{\rm h}/M_\odot) \sim 12.0$ and decrease with mass above. Note that upper limits on the O VI column densities from Kacprzak et al. (2015) and Pointon et al. (2017) are plotted for completeness, but they are not studied here since we focus on kinematics, which non-absorbers do not have by definition. The upper limits mostly lie below $\log N_{\rm O VI} = 13.7$ regardless of halo mass, indicating that the O VI CGM is inherently patchy. We leave further analysis to later work.

4. ABSORBER–GALAXY KINEMATICS

In this section we examine the relative absorber–galaxy kinematics using the TPCFs described in Section 2.3.2. Note that we normalize pixel–galaxy velocities by the circular velocity at the observed impact parameter, $V_{\rm c}(D)$, in order to assess the kinematics in a mass-independent way. This is done in light of the results of the previous section, which showed a significant mass-dependence in the absorber kinematics. We also only focus on isolated galaxy sightlines (i.e., no group environment kinematics from Figure 1) due to the velocity normalization. Since the O VI gas is in an intra-group medium and is not specifically associated with a particular galaxy, we cannot assign a single $V_{\rm c}(D)$ for each group absorber.

4.1. *Bivariate Analysis*

We again slice the sample by mass, but choose the median halo mass of the sample ($\langle\log(M_{\rm h}/M_\odot)\rangle = 11.88$) in order to have roughly equal numbers of galaxies in each mass bin for a later multivariate analysis. The absorber–galaxy TPCFs
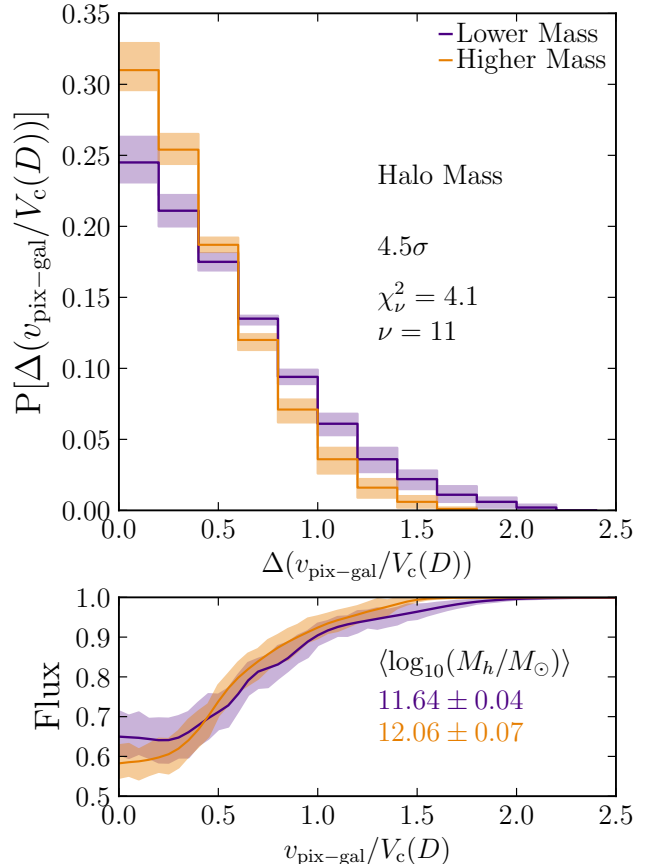

Figure 3. (Top) Normalized absorber–galaxy TPCFs for lower mass and higher mass galaxies. Unlike Figure 1, the pixel–galaxy velocities are normalized by the circular velocity at the observed impact parameter, $V_{\rm c}(D)$, to account for the range of halo masses in the sample. This shows a strong mass-dependence for the kinematics associated with O VI at the 4.5σ level, where lower mass galaxies have significantly larger velocity dispersions than higher mass galaxies. (Bottom) The average absorption spectra corresponding to lower mass galaxies and higher mass galaxies. 1σ uncertainties for both the TPCFs and average absorption spectra were calculated with a bootstrap analysis with 100 bootstrap realizations.

and associated average absorption profiles for lower mass and higher mass galaxies are plotted in Figure 3. After accounting for the inherent mass bias in the absorber kinematics above, we find that lower mass galaxies ($\log(M_{\rm h}/M_\odot) < 11.88$) have larger absorber–galaxy velocity dispersions compared with higher mass galaxies ($\log(M_{\rm h}/M_\odot) \geq 11.88$) at a significance of 4.5σ. From Table 2, $\Delta v(50)$ and $\Delta v(90)$ for lower mass galaxies ($0.45^{+0.03}_{-0.03}$ and $1.12^{+0.08}_{-0.09}$, respectively) are larger than that for higher mass galaxies ($0.34^{+0.019}_{-0.02}$ and $0.87^{+0.06}_{-0.07}$, respectively).

The average absorption profiles below the TPCFs in Figure 3 show that the bulk of the absorption lies around the galaxy systemic velocity, and this result applies to all subsequent subsample slices. Furthermore, most of the absorption lies within the host galaxy's circular velocity at the observed impact parameter, indicating that this gas is likely bound to the galaxy. In a complement to the TPCFs, the average absorption profile for lower mass galaxies extends to larger normalized pixel–galaxy velocities than for higher mass galaxies. This small fraction of the absorption profiles has velocities greater than $V_{\rm c}(D)$, indicating that this gas may not be bound to the host galaxies, and the fraction may be larger for lower
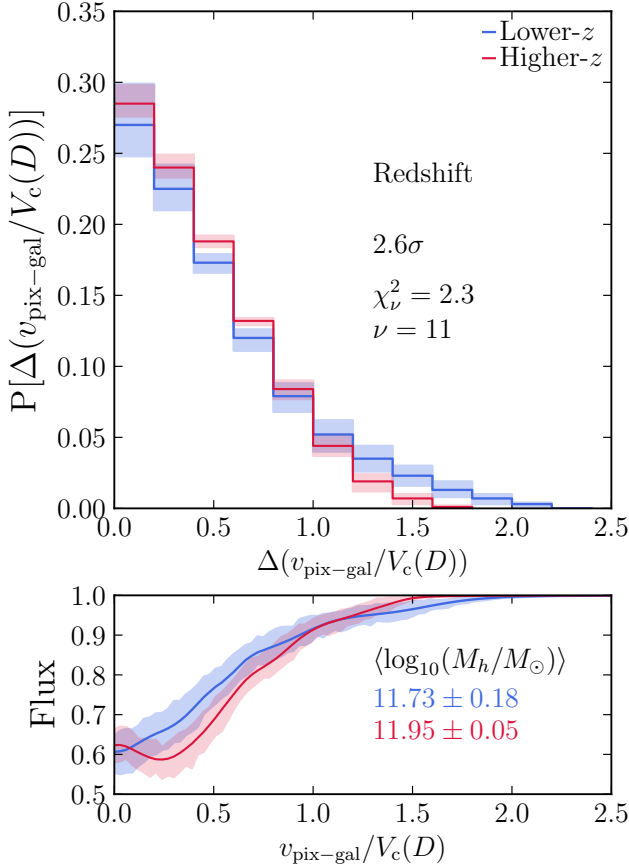
Figure 4. (Top) Normalized absorber–galaxy TPCFs for lower redshift and higher redshift galaxies. There is a probable redshift dependence of the O VI kinematics at the 2.6σ level, where O VI absorbing gas in lower redshift galaxies has larger velocities relative to O VI absorbing gas in higher redshift galaxies. (Bottom) The average absorption spectra corresponding to lower and higher redshift galaxies. 1σ uncertainties for both the TPCFs and the average spectra were calculated with a bootstrap analysis with 100 bootstrap realizations.

mass galaxies.

To account for any redshift evolution of the absorber–galaxy kinematics, we cut the sample by the median redshift, $\langle z_{\text{gal}} \rangle = 0.244$. This was motivated by work done in Nielsen et al. (2016), who found that the Mg II absorber velocity dispersions for red galaxies decreased with decreasing redshift, possibly indicative of the quenching of star formation. In Figure 4, there is a weak suggestion that lower redshift galaxies ($\langle z_{\text{gal}} \rangle < 0.244$) have larger absorber–galaxy velocity dispersions than higher redshift galaxies ($\langle z_{\text{gal}} \rangle \geq 0.244$) at a significance of 2.6σ. This result trends in the opposite direction as that found with Mg II, although here we are investigating the relative absorber–galaxy velocity dispersions rather than absorber velocity dispersions. Referring to Table 2, $\Delta v(50)$ measurements for lower redshift galaxies and higher redshift galaxies are similar, although $\Delta v(90)$ for lower redshift galaxies is slightly larger than for higher redshift galaxies. The median masses for the two subsamples are consistent within uncertainties, so any differences seen here are likely not dominated by the mass dependence of Figure 3. The average absorption profiles in the bottom panel of Figure 4 show that lower redshift galaxies have a nontrivial optical depth at a larger normalized pixel–galaxy velocity compared with the higher redshift galaxies, but the two profiles are still consis-

tent within uncertainties. It is possible that O VI kinematics have a redshift dependence, analogous to that of Mg II kinematics in red galaxies (Nielsen et al. 2016), but this investigation would be better done on a sample with a greater range in redshifts (up to $z \sim 2-3$).

We also cut the sample by the median inclination, $\langle i \rangle = 51°$, where galaxies with $i \geq 51°$ are considered "edge-on" galaxies and galaxies with $i < 51°$ are considered "face-on" galaxies. We find that both edge-on and face-on galaxies have the same velocity dispersions (0.01σ, not plotted) and average absorption profiles. The $\Delta v(50)$ and $\Delta v(90)$ measurements reported in Table 2 are consistent within uncertainties. The median masses and median redshifts for the two subsamples are consistent within uncertainties.

A final bivariate cut made to the sample is the median azimuthal angle of $\langle \Phi \rangle = 45°$, where galaxies with $\Phi \geq 45°$ are considered "minor axis" galaxies, that is, galaxies that are probed along their projected minor axis. "Major axis" galaxies, where $\Phi < 45°$, are defined in a similar fashion. We find that minor axis galaxies have similar velocity dispersions to major axis galaxies (1.5σ, not plotted), and the average absorption profiles are not qualitatively different. From Table 2, the $\Delta v(50)$ and $\Delta v(90)$ measurements for both major axis galaxies and minor axis galaxies are inconsistent within uncertainties, but are still within 1.4σ. Additionally, the median masses and median redshifts for the major axis galaxies and minor axis galaxies are consistent within errors.

The independence of the O VI kinematics on the inclination and azimuthal angles reported here has been confirmed in previous work (Nielsen et al. 2017; Kacprzak et al. 2019), but here we have obtained the same conclusion with absorber–galaxy kinematics for simple bivariate cuts.

4.2. *Multivariate Analysis*

4.2.1. *Inclination and Azimuthal Angle*

In Figure 5, we present the TPCFs for galaxy subsamples cut by inclination, i, as well as galaxy azimuthal angle, Φ, for all halo masses. The corresponding average absorption profiles are plotted in the panels below the TPCFs.

In Figure 5(a), we compare face-on (cyan lines) and edge-on (orange lines) galaxies probed along their projected major axis. There is no difference in the absorber–galaxy velocity dispersions between the two inclinations (0.1σ). The associated $\Delta v(50)$ and $\Delta v(90)$ measurements presented in Table 2 are consistent within uncertainties, providing further support that the velocity dispersions between face-on and edge-on inclinations for major axis galaxies are very similar. The median masses for the two subsamples are consistent within uncertainties. The average absorption profile shows that there is a slight tail for the edge-on, major axis galaxies at higher normalized pixel–galaxy velocities. While this is reflected in the TPCFs, the difference between the plotted subsamples is not significant due to large uncertainties. There is also more optical depth near the galaxy systemic velocity for the face-on, major axis galaxies compared with the edge-on, major axis galaxies.

Figure 5(b) compares face-on (cyan lines) and edge-on (orange lines) inclinations as well, but for galaxies probed along their projected minor axis. There is a significant difference in the velocity dispersions between the two inclinations (3.1σ), where face-on galaxies probed along the minor axis have a slightly larger velocity dispersion than edge-on galaxies. From Table 2, the associated $\Delta v(50)$ measurements
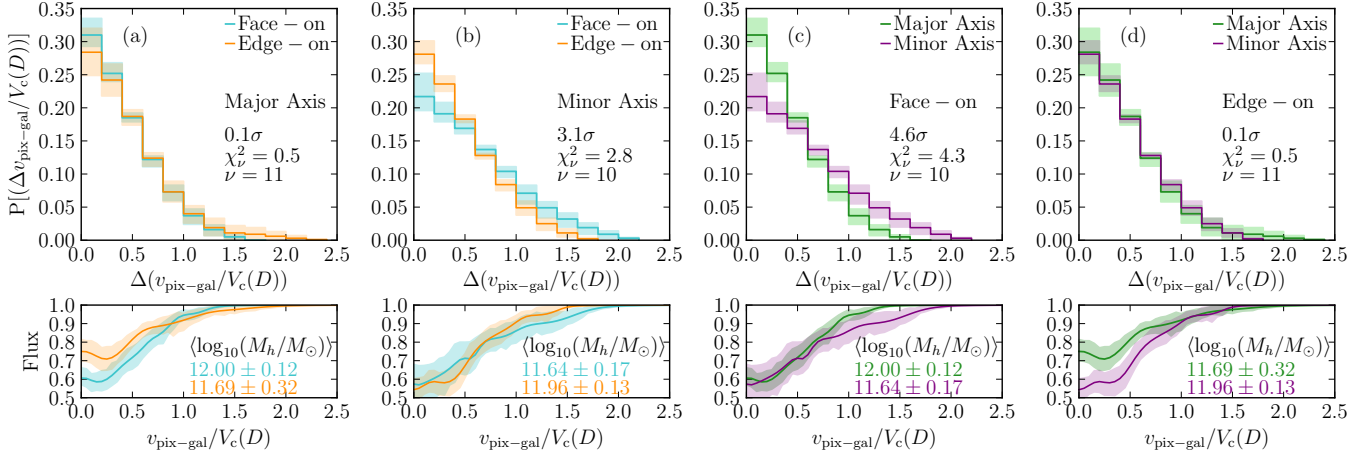
Figure 5. (Top) Normalized absorber–galaxy TPCFs for a) edge-on and face-on galaxies probed along the major axis; b) edge-on and face-on galaxies probed along the minor axis; c) face-on galaxies probed along the major and minor axes; d) edge-on galaxies probed along the major and minor axes. (Bottom) Average absorption profiles corresponding to the top panels. In a) and b), cyan corresponds to face-on galaxies, and orange corresponds to edge-on galaxies. In c) and d), green corresponds to galaxies probed along the major axis, and purple corresponds to galaxies probed along the minor axis. The uncertainties for the average absorption profiles were calculated with a bootstrap analysis with 100 bootstrap realizations.

for face-on, minor axis galaxies ($0.51^{+0.04}_{-0.06}$) are larger than for edge-on, minor axis galaxies ($0.38^{+0.02}_{-0.03}$). Additionally, $\Delta v(90)$ for face-on, minor axis galaxies ($1.24^{+0.10}_{-0.16}$) is larger than for edge-on, minor axis galaxies ($0.96^{+0.07}_{-0.08}$). This may be attributable to the observation that edge-on, minor axis galaxies ($\langle\log(M_{\rm h}/M_\odot)\rangle = 11.96 \pm 0.13$) tend to be of higher mass than that of face-on, minor axis galaxies ($\langle\log(M_{\rm h}/M_\odot)\rangle = 11.64 \pm 0.17$), so the corresponding halos have a larger virial temperature. This provides the conditions for O VI to ionize into higher order species and thus reduces the size and kinematic extent of the O VI clouds (Oppenheimer et al. 2016; Pointon et al. 2017). The average absorption profiles clearly show that there is a larger optical depth at higher normalized velocities for the face-on, minor axis galaxies compared with the edge-on, minor axis galaxies. This is seen as the tail in the TPCF, but the uncertainties in the TPCFs are large. The average absorption profile shows no differences in the absorption between the two subsamples around the galaxy systemic velocity.

Figure 5(c) compares face-on galaxies probed along the major axis (green lines) and minor axis (purple lines). There is a very significant difference (4.6σ) in the velocity dispersions, with minor axis galaxies showing a larger velocity dispersion compared with major axis galaxies in face-on ($i < 51°$) inclinations. This is also seen in the $\Delta v(50)$ and $\Delta v(90)$ measurements reported in Table 2, where $\Delta v(50)$ for face-on galaxies probed along the minor axis ($0.51^{+0.04}_{-0.06}$) is significantly larger than when probed along the major axis ($0.35^{+0.02}_{-0.03}$). Likewise, the $\Delta v(90)$ value for face-on galaxies probed along the minor axis ($1.24^{+0.10}_{-0.16}$) is significantly larger than face-on galaxies probed along the major axis ($0.87^{+0.06}_{-0.09}$). The median mass for face-on, minor axis galaxies, $\langle\log(M_{\rm h}/M_\odot)\rangle = 11.64 \pm 0.17$, is lower than that for face-on, major axis galaxies, $\langle\log(M_{\rm h}/M_\odot)\rangle = 12.00 \pm 0.12$, where the direction of the difference reflects the result of Figure 3. The mass difference likely plays a role in the significant difference in the TPCFs, rather than being only an inclination effect. The average absorption profile also shows a much larger optical depth at higher normalized velocities (largely for $v_{\rm pix-gal}/V_{\rm c}(D) > 1$, where the gas is more likely to be unbound) for face-on, minor

axis galaxies compared with the face-on, major axis galaxies, which is seen as the tail in the TPCF. Where the gas is expected to be bound, there is no difference in the average absorption profiles around the galaxy systemic velocity.

Finally, Figure 5(d) compares edge-on galaxies probed along the major axis (green lines) and minor axis (purple lines). There is no difference (0.1σ) in the velocity dispersions between the two azimuthal angle categories. This is reflected in the overlap of the respective $\Delta v(50)$ and $\Delta v(90)$ measurements reported in Table 2. The median masses for edge-on, major axis galaxies and edge-on, minor axis galaxies are consistent within uncertainties. The average absorption profiles also have similar optical depths at the larger normalized velocities, but there is a larger optical depth for the edge-on, minor axis galaxies around the galaxy systemic velocity compared with the edge-on, major axis galaxies.

4.2.2. *Halo Masses and Orientation*

Given the significant difference in the absorber–galaxy kinematics for lower mass galaxies compared to higher mass galaxies, the results in the previous section with galaxy inclinations and azimuthal angles may largely be due to the distribution of galaxy masses in each subsample comparison. In Figure 6, we present TPCFs for galaxy subsamples cut by halo mass, $\log(M_{\rm h}/M_\odot)$, and one of two galaxy orientation measures: inclination, i, or azimuthal angle, Φ. The corresponding average absorption profiles are plotted in the panels below the TPCFs. We conduct this test to better pinpoint the galaxy properties that are most important in governing the absorber–galaxy kinematics.

Figure 6(a) compares lower mass (indigo lines) and higher mass (orange lines) galaxies probed along the major axis. There is no difference (1.0σ) in the velocity dispersions, though the lower mass galaxies have a slightly wider velocity dispersion tail (but with large uncertainties) than higher mass galaxies when probed along the major axis. This is reflected in the consistency, within uncertainties, of the $\Delta v(50)$ and $\Delta v(90)$ measurements from Table 2 between the two subsamples. The average absorption profiles are also consistent within uncertainties.

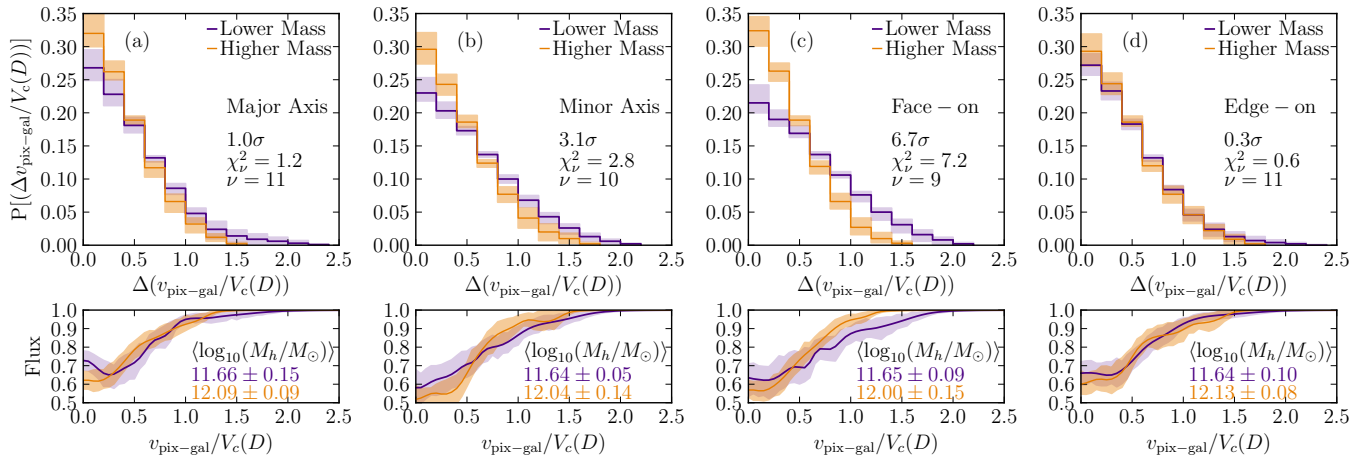Figure 6(b) shows the TPCFs for minor axis galaxies. There

Figure 6. (Top) Normalized absorber–galaxy TPCFs for lower mass and higher mass galaxies probed along a) the major axis; b) the minor axis, and seen in c) face-on inclinations; d) edge-on inclinations. (Bottom) Average absorption profiles corresponding to the top panels. Orange corresponds to higher mass galaxies, and purple corresponds to lower mass galaxies. The uncertainties were calculated with a bootstrap analysis with 100 bootstrap realizations.

is a significant difference (3.1σ) between the velocity dispersions of the lower mass (indigo lines) and higher mass (orange lines) galaxies, where lower mass galaxies have a larger velocity dispersion than higher mass galaxies probed along the minor axis. The difference in velocity dispersions is also seen in the $\Delta v(50)$ and $\Delta v(90)$ measurements reported in Table 2, where these values for lower mass galaxies ($0.48^{+0.03}_{-0.04}$ and $1.17^{+0.07}_{-0.11}$, respectively) are larger than for higher mass galaxies ($0.37^{+0.03}_{-0.03}$ and $0.90^{+0.10}_{-0.11}$, respectively). While this difference was expected from Figure 3, the fact that the comparison for galaxies probed along the projected major axis in Figure 6(a) is insignificant indicates that azimuthal angle plays a role in the observed kinematic structure. However, the average absorption profiles for the two subsamples are comparable within uncertainties.

In Figure 6(c), we compare lower and higher mass TPCFs for face-on galaxies. There is a very significant difference (6.7σ) between the velocity dispersions of the lower mass (indigo lines) and higher mass (orange lines) galaxies, where lower mass, face-on galaxies have a much larger velocity dispersion than higher mass, face-on galaxies. The difference in velocity dispersions is reflected in the $\Delta v(50)$ and $\Delta v(90)$ measurements from Table 2, where the values for the lower mass, face-on galaxies ($0.51^{+0.03}_{-0.05}$ and $1.23^{+0.08}_{-0.14}$, respectively) are much greater than for higher mass, face-on galaxies ($0.33^{+0.03}_{-0.02}$ and $0.81^{+0.08}_{-0.06}$). The average absorption profiles also show that the optical depth at higher normalized velocities is much larger for the lower mass, face-on galaxies compared with the higher mass, face-on galaxies.

In Figure 6(d), we compare the TPCFs of lower mass and higher mass galaxies with edge-on inclinations. There is no difference (0.3σ) between the velocity dispersions of the lower mass, edge-on (indigo lines) and higher mass, edge-on (orange lines) galaxies. This is seen in the consistency between their $\Delta v(50)$ and $\Delta v(90)$ measurements. The mass-dependence found in Figure 3 is not present for edge-on galaxies, but is for face-on galaxies in the previous paragraph, suggesting that galaxy inclination is important for determining the absorber–galaxy kinematics. The average absorption profile of the lower mass, edge-on galaxies and the higher mass, edge-on galaxies are very similar, where the bulk of the absorption occurs around the galaxy systemic velocity, and

the optical depth tapers off at similar normalized velocities.

Finally, we tested similar mass bins for the orientation subsamples, although these comparisons are not plotted directly. There are no significant differences between major and minor axis galaxies for either the lower mass (0.8σ) or higher mass (0.4σ) subsamples. Similarly, there is no significant difference between edge-on and face-on galaxies for the higher mass subsample. However, face-on lower mass galaxies have significantly larger velocity dispersions compared to edge-on lower mass galaxies (3.3σ). In this section, the clear outlier in kinematics is thus the lower mass, face-on subsample.

5. DISCUSSION

From the TPCFs and average absorption profiles presented above, we find that there is a strong mass dependence of the O VI absorber kinematics, where higher mass ($\log(M_{\rm h}/M_\odot) \geq 11.7$) isolated galaxies have larger velocity dispersions compared with lower mass ($\log(M_{\rm h}/M_\odot) < 11.7$) isolated galaxies. Group galaxies have much narrower velocity dispersions than the higher mass isolated galaxies (13.1σ). We also find that the absorber–galaxy kinematics display non-virialized motions, primarily due to possible outflows in face-on and minor axis orientations particularly for lower mass galaxies. These were found after normalizing the pixel–galaxy velocities by the circular velocity at the observed impact parameter, $V_{\rm c}(D)$, to account for the range of halo masses in the sample.

5.1. *Absorber Kinematics*

The mass dependence of the TPCFs and average absorption profiles in Figure 1 may be attributable to the strength of the O VI absorption, quantified by the column density, $\log N_{\rm OVI}$. Simulations of O VI in galaxy halos show that the column density reaches its apex at $\log(M_{\rm h}/M_\odot) = 12$ because the virial temperature of these galaxies is comparable to the temperature at which the O VI ionization fraction is greatest (Oppenheimer et al. 2016; also see Nelson et al. 2018 and Oppenheimer et al. 2018 for an alternative explanation). Galaxy halos with lower ($\log(M_{\rm h}/M_\odot) < 11.7$) or higher masses ($\log(M_{\rm h}/M_\odot) > 12.3$, i.e., group environments) have lower column densities or weaker O VI absorption. This is likely because a smaller (larger) galaxy halo mass corresponds to a halo that is too cold (hot) for a significant fraction of O VI. We confirm this trend in the observational column densities plot-

ted in Figure 2. This relation may also lead to smaller O VI clouds and a statistically lower kinematic extent for sub-L^* and group galaxies.

We clearly see this effect in the absorber kinematics. The median mass for higher mass galaxies corresponds to $\sim L^*$ galaxies, which have a virial temperature that is most conducive for the presence of O VI gas according to Oppenheimer et al. (2016). Our results indicate that this also leads to a larger kinematic extent of the O VI gas since there is more gas to be distributed along the line of sight. In contrast, lower mass galaxies at sub-L^* likely have virial temperatures which are too cool for a significant presence of O VI, resulting in more narrow kinematic dispersions. As shown by Pointon et al. (2017) and confirmed here, group galaxies are the other extreme in that they likely live in halos with virial temperatures that are too warm for O VI. As O VI ionizes out into higher order species (e.g., O VII and beyond) for these highest mass galaxies, this translates to narrower kinematic extents. While this result was presented in Pointon et al. (2017), we have now shown the change in the O VI kinematics for all three mass bins corresponding to the simulation results, which the previous work had not done since they were focused on the difference between isolated and group galaxies.

We also saw this mass-O VI effect in the optical depth distribution of the average absorption profiles. For all pixel velocities, higher mass galaxies ($\log(M_h/M_\odot) \approx 12$) have more absorption compared to both lower mass galaxies ($\log(M_h/M_\odot) < 11.7$) and group environments ($\log(M_h/M_\odot) \gtrsim 12.3$). As shown in Figure 2, the column densities obtained from these average absorption profiles, $\log N_{O VI} = 14.436, 14.570$, and 14.18 for increasing halo mass, are comparable to but slightly larger than the aperture column densities obtained by Oppenheimer et al. (2016) in the EAGLE simulations.

Previous absorber kinematics work by Nielsen et al. (2017) did not investigate this mass dependence, rather they focused on the star formation properties of the galaxies with $B-K$ colors. They found that the kinematics did not depend on galaxy orientations or star formation activity and suggested that the observed gas may be a result of ancient outflows which have had time to form a roughly kinematically uniform halo. They also suggested that differing ionization conditions throughout the CGM result in the azimuthal angle dependence of O VI found by Kacprzak et al. (2015). Combined with the results presented here, we suggest that the absorption properties of O VI are not good probes of current baryon cycle processes in galaxies, but are instead primarily probes of halo mass.

5.2. *Absorber–Galaxy Kinematics*

Since we normalized the pixel–galaxy velocities by the galaxy circular velocity at the observed impact parameter, $V_c(D)$, the absorber–galaxy kinematics of the isolated galaxy sample are effectively mass-independent. Thus the differences between subsamples for the absorber–galaxy kinematics should not be dominated by mass and, due to studying the relative velocities between the observed gas and the host galaxies, may reflect baryon cycle processes.

We first tested this by examining the relative absorber–galaxy kinematics for lower and higher mass galaxies in Figure 3. Overall, the bulk of the absorption lies near the galaxy systemic velocity, with little gas exceeding the galaxy circular velocity, similar to previous work comparing to the galaxy escape velocity (Tumlinson et al. 2011; Mathes et al. 2014; Kacprzak et al. 2019). The small fraction of gas that does ex-

ceed $V_c(D)$ is more likely to escape the galaxy, and this fraction is slightly larger for lower mass galaxies, which have statistically larger (4.5σ) absorber–galaxy kinematics. Mathes et al. (2014) examined a sample of 11 galaxies with measured O VI absorption and found that the gas around lower mass galaxies is more likely to escape the halo than higher mass galaxies. The authors suggested this is evidence for differential kinematics due to differential wind recycling, where outflowing gas in higher mass galaxies is more likely to recycle back onto the host galaxy (Oppenheimer et al. 2010). Furthermore, Mathes et al. (2014) also presented CGM radial velocities for a simulated $\log(M_h/M_\odot) \simeq 11.3$ galaxy. While radially infalling gas rarely exceeded $V_c(D)$ beyond 40 kpc, outflowing gas often exceeded this value out to at least 140 kpc. This suggests that some portion of O VI traces outflowing gas and that the absorber–galaxy kinematics are the probe needed to detect these gas flows.

We examined this further by studying the kinematics as a function of galaxy orientation, where outflows are expected to dominate sightlines probing galaxies along their projected minor axis or probing face-on galaxies. We compared the kinematics for face-on galaxies to edge-on galaxies and found that there is no significant difference (0σ) in the velocity dispersions or the average absorption profiles. A similar result was found when comparing galaxies probed along the projected major axis to those probed along the projected minor axis (1.5σ). This is likely due to other factors such as comparable halo masses between the subsamples and the fact that outflows are not expected along the projected major axis of edge-on galaxies, or for major axis galaxies with inclinations closer to being face-on. Thus, we sliced the sample further.

While O VI is often associated with ancient outflows (e.g., Ford et al. 2014), we focus first on galaxy orientation subsamples in which outflows are not expected to dominate the kinematic signatures. Accretion/rotation line-of-sight velocities are maximized for edge-on galaxies along the major axis (at least for low impact parameter, e.g., Steidel et al. 2002; Kacprzak et al. 2010; Stewart et al. 2011; Danovich et al. 2012, 2015), whereas outflow velocities are minimized (e.g., Rubin et al. 2014). In Figure 5(a), we found no significant difference in the absorber–galaxy TPCFs between face-on galaxies and edge-on galaxies probed along their projected major axes (0.1σ). However, while the average absorption profiles taper off at similar normalized pixel–galaxy velocities within uncertainties, the optical depths differ within $v_{pix-gal}/V_c(D) = 0.5$ of the galaxy systemic velocity. There is less absorption at these velocities for edge-on galaxies than face-on galaxies. To better understand this result, we compare edge-on galaxies probed along their major and minor axes in Figure 5(d). The TPCFs for the two subsamples are again consistent (0.1σ), but there is less absorption at low normalized pixel-velocity values for the major axis subsample.

These results are likely not due to halo mass since the subsamples in both comparisons have similar median halo masses, although the edge-on subsample does trend toward lower masses. Rather, they are likely due to the finding that, other than the halo mass (and therefore virial temperature), O VI is expected to largely trace ancient outflows instead of accreting gas. In an edge-on inclination, outflows manifest as minor axis absorption centered around the galaxy systemic velocity since the radial velocity component is mostly perpendicular to a galaxy's disk. Therefore, there is likely more gas along the minor axis, with very little along the major axis where accreting gas is preferred. Furthermore, the quasar

sightline technique introduces problems for interpreting O VI gas origins. Recently, Kacprzak et al. (2019) examined the relative velocities between O VI and the host galaxy rotation curves for absorbers along the projected major axis. They found that O VI does not correlate with galaxy rotation. Instead, the ion has velocity dispersions that span the entire range of galaxy rotation velocities. However, the authors did find inflowing O VI filaments in the CGM of simulated galaxies. The discrepancy between the observed and simulated data comes in the form of the quasar sightlines, where the observed kinematic signatures of gas infall are blurred due to multiple kinematic structures along the lines-of-sight which cannot be disentangled with the data currently available (also see Churchill et al. 2015; Peeples et al. 2018). Also note that O VI absorbing clouds are predicted to be large, with radii on the order of tens to hundreds of kiloparsecs from photoionization modeling (Lopez et al. 2007; Muzahid 2014; Hussain et al. 2015; Stern et al. 2016).[2] This is particularly important given that accreting filaments tend to have small covering fractions (e.g., Martin et al. 2012; Rubin et al. 2012).

We now focus on orientations in which outflows are expected to dominate kinematic signatures: face-on galaxies and galaxies probed along their projected minor axes. In Figure 5(b), there is a significant difference between face-on and edge-on galaxies probed along the minor axis (3.1σ), where the velocity dispersions are larger for face-on galaxies. The significance is not very strong, but this may be due to the fact that both subsamples trace outflowing gas. The edge-on minor axis kinematics likely have smaller velocity dispersions because the outflow velocities are minimized in edge-on inclinations but are maximized for face-on inclinations. The average absorption profiles are similar within uncertainties, but there is a suggestion that the edge-on subsample is more centrally concentrated near the galaxy systemic velocity, as expected for a bipolar outflow geometry. The optical depth profile is more smooth for the face-on subsample out to large normalized pixel velocities, likely reflecting varying outflowing velocities with impact parameter. This is supported by the results of Kacprzak et al. (2019), who also investigated minor axis O VI and found that this observed gas can largely be modeled by a decelerating outflow. The gas may flow away from the host galaxy, slowing down and building up the amount of gas as it outflows, which then eventually falls back onto the galaxy. Thus, the full range of outflow velocities is observed in the absorber–galaxy kinematics of face-on minor axis orientations.

A highly significant difference is also present in Figure 5(c), which compares face-on galaxies probed along the projected major axis versus the projected minor axis (4.6σ), where face-on minor axis galaxies have large velocity dispersions. Recall that "face-on" here means $i < 51°$ but 9/10 face-on, major axis galaxies have $25° < i < 51°$. In this TPCF comparison, only the minor axis sightlines are expected to be dominated by outflows unless the opening angle of outflows is large. The O VI outflow half-opening angle appears to have a range of $30° - 50°$ (Kacprzak et al. 2015), so major axis sightlines may pass through outflowing gas, but the kinematics suggest that they do not encounter a significant amount of recent outflows. Also note that the face-on minor axis subsample has a larger impact parameter on average, $\langle D \rangle = 95.7$ kpc, than the face-

on major axis subsample, $\langle D \rangle = 75.6$ kpc.[3] The influence of outflows is expected to be greater at lower impact parameter, so the fact that there are significantly smaller velocity dispersions for the absorber–galaxy kinematics in the major axis subsample again indicates that outflows do not dominate the absorption signature here. However, the combination of large absorber–galaxy velocity dispersions and large impact parameters along the minor axis is interesting given the simulation results presented in Kacprzak et al. (2019). The authors found that for simulated galaxies at $z = 1$ with $\log(M_h/M_\odot) \sim 11.7$, minor axis O VI outflows accelerate out to $D \sim 50$ kpc, where the gas begins to decelerate and later falls back onto the host galaxy. Perhaps the larger mean impact parameter for our minor axis face-on sample reflects the build-up of O VI gas due to this velocity turn-over, making the gas more easily observed.

As discussed in Section 5.1, we found a significant mass dependence of the absorber kinematics, which was normalized out for the absorber–galaxy kinematics. In the subsequent discussion, we assumed that halo mass no longer had a large part to play in the observed differences. To further show that mass does not exclusively control the absorber–galaxy kinematics (in contrast to the absorber kinematics), we point to Figure 6. If mass was the most important galaxy property governing the kinematics even after normalizing by $V_c(D)$, then every panel in the Figure would show significant differences given that the comparisons are between lower and higher mass. However, this is not the case. The only significant differences found are for comparisons in which outflows are expected to dominate the kinematics. Most importantly, the lower mass face-on galaxy subsample is the outlier, with large absorber–galaxy velocity dispersions that are significantly larger than both higher mass face-on galaxies (6.7σ) and lower mass edge-on galaxies (3.3σ).

The ease at which outflowing gas signatures are observed in lower mass face-on galaxies could be explained via one or both of the following: 1) There is a bias in the subsamples being compared. In this case, the lower mass face-on subsample is dominated by sightlines probing the galaxies along their projected minor axes (four out of six sightlines), whereas the higher mass face-on subsample is dominated by sightlines probing projected major axes (eight out of nine sightlines). 2) The large velocity dispersions are physical and may be due to a combination of the orientation at which the gas is being probed and the halo mass.

Some of the issues in case (1) may be resolved when considering that Rubin et al. (2014) found that down-the-barrel Mg II outflows are most easily observed for face-on inclinations (detection rate of $\sim 89\%$ compared to $\sim 45\%$ for edge-on galaxies), *with no consideration of the azimuthal angle*, and it is reasonable to expect similar detection rates for O VI outflows in similar inclinations. Therefore, one would expect to see similar outflow signatures in face-on galaxies regardless of the azimuthal angle in our sample. This is not the case here. Furthermore, the authors found no significant dependence of the outflow detection rate on galaxy mass, finding outflows across all stellar masses in their sample, in contrast to the results we present here. It appears that the bias described in case (1) is not the cause for our absorber–galaxy kinematic differences. While a sample with a better distribution of galaxy properties would improve this study, it is beyond the scope of

---

[2] Though note that the Oppenheimer et al. (2016) results assume O VI is collisionally ionized. It is more likely that O VI is some combination of photoionized and collisionally ionized.

[3] The mean impact parameters for the edge-on major axis and minor axis subsamples are both $\langle D \rangle \sim 109$ kpc. This would be expected in the case of a uniform halo of O VI absorbing gas.

this paper.

For case (2) in which the large velocity dispersions are physical, recall that face-on inclinations result in maximized outflow velocities along the line-of-sight. Combined with the high detection rate in face-on inclinations described above, the large absorber–galaxy velocity dispersions observed in our face-on subsamples (lower mass and edge-on galaxies) are likely evidence of outflows. As for the mass-dependence in case (2), the specific star formation rate is expected to be larger for lower mass galaxies, where lower mass galaxies are more likely to be actively creating their stellar populations from recent star formation (e.g., Feulner et al. 2005). In this instance, outflowing gas in lower mass galaxies is likely more recent, which reduces the amount of time available for O VI gas to kinematically mix within the CGM (evidence for this kinematic mixing of O VI is discussed in Nielsen et al. 2017 and "kinematic blurring" arguments due to many line-of-sight structures are detailed in Kacprzak et al. 2019). Thus, the kinematic signatures of outflows along the line-of-sight are more likely to be preserved for lower mass galaxies than higher mass galaxies.

6. SUMMARY AND CONCLUSIONS

We first examined the absorber kinematics for O VI with the TPCF method employed in Nielsen et al. (2015, 2016, 2017, 2018); Pointon et al. (2017). The rest of the work analyzed absorber–galaxy kinematics for O VI gas using a modified version of the TPCFs. We used a subset of 31 galaxies from the "Multiphase Galaxy Halos" Survey (Kacprzak et al. 2015, 2019; Muzahid et al. 2015, 2016; Nielsen et al. 2017; Pointon et al. 2017, 2019) for the TPCF analysis; these are isolated galaxies, where they have no neighboring galaxies within 200 kpc and within a line-of-sight velocity separation of 500 km s^{-1}. The galaxies span $0.13 < z_{gal} < 0.66$, where σ_z is better than ~ 30 km s^{-1} (e.g., Kacprzak et al. 2019) and are found within a projected distance of 200 kpc from the quasar sightline. The galaxies were imaged with ACS, WFC3 or WFPC2 on *HST*, and the associated morphological properties were modeled using GIM2D (Simard et al. 2002; Kacprzak et al. 2015).

We shifted the pixel velocities from the absorption spectra relative to the galaxy systemic velocities, and normalized them with respect to the circular velocity at the impact parameter, $V_c(D)$, to account for a range of halo masses ($10.9 \leq \log(M_h/M_\odot) \leq 12.5$) in the sample. We also found that this was crucial to eliminate any potential mass biases in the results. We analyzed absorber–galaxy kinematics of the subsamples derived from cuts by the halo mass, $\log(M_h/M_\odot)$, galaxy redshift, z_{gal}, azimuthal angle, Φ, and inclination, i. The TPCFs are supplemented by average absorption profiles, which provide optical depth distribution information.

We thus find that:

1. There is a mass dependence in the O VI absorber kinematics consistent with the column density–mass trends of Oppenheimer et al. (2016). Lower mass galaxies ($\log(M_h/M_\odot) < 11.7$) tend to have narrower velocity dispersions than the typically more massive galaxies ($\log(M_h/M_\odot) \sim 12$). Subsamples with halo masses consistent with L^* galaxies tend to have the largest velocity dispersions and this is reflected in both the TPCFs and the average absorption profiles. This mass subsample coincides with that of maximum O VI column density due to having a virial temperature com-

parable to the temperature at which the O VI ionization fraction is greatest. The largest halo masses, the group environment sample from Pointon et al. (2017), have the smallest velocity dispersions. This is likely due to more massive halos having a larger virial temperature, which provides the environment for O VI to be promoted to higher order species (e.g., O VII and beyond). The most massive halos are too hot for large O VI ionization fractions, thus reducing the size of O VI clouds and statistically leading to narrower kinematic extents.

2. The total O VI column densities for the lower mass, higher mass, and group samples are consistent with the aperture column densities from Oppenheimer et al. (2016), for $\log(M_h/M_\odot) \geq 10.9$. This result provides further observational evidence of the virial temperature dependence of O VI.

3. After normalizing absorber–galaxy TPCFs by the circular velocity at the observed impact parameter, $V_c(D)$, to account for halo mass, we found that lower mass galaxies ($\langle \log(M_h/M_\odot) \rangle = 11.64$) have significantly larger (4.5σ) absorber–galaxy velocity dispersions compared to higher mass galaxies ($\langle \log(M_h/M_\odot) \rangle = 12.06$). The average absorption profiles demonstrate that there is a larger fraction of gas with velocities greater than $V_c(D)$ for the lower mass subsample, suggestive of outflowing gas (e.g., Oppenheimer et al. 2010; Mathes et al. 2014; Kacprzak et al. 2019).

4. There are no significant differences for bivariate comparisons with subsamples sliced only by galaxy redshift (2.6σ), inclination (0.01σ), or azimuthal angle (1.5σ). However, these simple cuts neglect the fact that, e.g., gas along the projected major and minor axes of edge-on galaxies is expected to exhibit different kinematic signatures (e.g., Steidel et al. 2002; Kacprzak et al. 2010; Stewart et al. 2011; Bouché et al. 2013).

5. A multivariate analysis investigating subsamples sliced by galaxy inclination angle and azimuthal angle shows potential outflow signatures. Large velocity dispersions and optical depths beyond $V_c(D)$ are found for orientations in which outflows are expected to be most optimal. Face-on minor axis subsamples have the largest kinematic dispersions and a smoothly decreasing optical depth distribution out to large normalized velocities, reflecting outflowing gas that is likely decelerating and will eventually return to the galaxy. Edge-on minor axis gas has large optical depths that are concentrated near the galaxy systemic velocity, suggesting a large quantity of O VI-absorbing gas being ejected perpendicular to the galaxy disk as expected for bipolar outflows. Accreting gas signatures are not directly observed for any subsample due to a combination of low covering fraction (e.g., Martin et al. 2012; Rubin et al. 2012) and "kinematic blurring" along the line-of-sight in which multiple kinematic structures are probed (e.g., Churchill et al. 2015; Peeples et al. 2018; Kacprzak et al. 2019).

6. Combining the mass and galaxy orientation subsamples, we found that while outflows are most easily observed in lower mass galaxies, the clear outlying subsample is lower mass face-on galaxies. In this case, more recent star formation in the lower mass galaxies than would be expected in higher mass galaxies results in the O VI gas having less time to mix kinematically to

obscure the expected kinematic signatures of outflows.

With these results, we suggest that in order to understand the physics of O VI-absorbing gas, it is imperative to first consider the halo mass of the host galaxy. Combining the results of Nielsen et al. (2017) and those presented in Section 3, O VI absorber kinematics largely represent the underlying virial temperature of the host halo rather than baryon cycle processes, unlike lower ions such as Mg II (Nielsen et al. 2016, 2015). Furthermore, accounting for the Kacprzak et al. (2019) results for a subset of galaxies presented here, studying the circular velocity-normalized absorber–galaxy kinematics of O VI shows indications of outflow signatures, but the kinematic blurring due to multiple structures along the line-of-sight and the large cloud sizes predicted for O VI from photoionization models rule out easily detecting accreting gas. Due to this, it is becoming increasingly important for simulations to accurately model the CGM in order to better understand the origins of the observed gas, and therefore better understand how galaxies cycle their gas.

Facilities: Keck:II (ESI)

REFERENCES

Alonso, S., Mesa, V., Padilla, N., & Lambas, D. G. 2012, A&A, 539, A46
Bordoloi, R., Lilly, S. J., Hardmeier, E., et al. 2014, ApJ, 794, 130
Bouché, N., Hohensee, W., Vargas, R., et al. 2012, MNRAS, 426, 801
Bouché, N., Murphy, M. T., Kacprzak, G. G., et al. 2013, Science, 341, 50
Bryan, G. L., & Norman, M. L. 1998, ApJ, 495, 80
Butler, M. J., Tan, J. C., Teyssier, R., et al. 2017, ApJ, 841, 82
Carswell, R. F., & Webb, J. K. 2014, VPFIT: Voigt profile fitting program, Astrophysics Source Code Library
Chen, H.-W., Lanzetta, K. M., & Webb, J. K. 2001, ApJ, 556, 158

Churchill, C. W., Mellon, R. R., Charlton, J. C., et al. 2000, ApJS, 130, 91
Churchill, C. W., Trujillo-Gomez, S., Nielsen, N. M., & Kacprzak, G. G. 2013, ApJ, 779, 87
Churchill, C. W., Vander Vliet, J. R., Trujillo-Gomez, S., Kacprzak, G. G., & Klypin, A. 2015, ApJ, 802, 10
Cole, S., Lacey, C. G., Baugh, C. M., & Frenk, C. S. 2000, MNRAS, 319, 168
Cooper, T. J., Simcoe, R. A., Cooksey, K. L., O'Meara, J. M., & Torrey, P. 2015, ApJ, 812, 58
Correa, C. A., Schaye, J., van de Voort, F., Duffy, A. R., & Wyithe, J. S. B. 2018, MNRAS
Cox, T. J., Jonsson, P., Somerville, R. S., Primack, J. R., & Dekel, A. 2008, MNRAS, 384, 386
da Costa-Luis, C., L., S., Mary, H., et al. 2018, tqdm/tqdm: tqdm v4.23.4 stable
Danovich, M., Dekel, A., Hahn, O., Ceverino, D., & Primack, J. 2015, MNRAS, 449, 2087
Danovich, M., Dekel, A., Hahn, O., & Teyssier, R. 2012, MNRAS, 422, 1732
Fernández, M., Yuan, F., Shen, S., et al. 2015, Galaxies, 3, 156
Feulner, G., Gabasch, A., Salvato, M., et al. 2005, ApJ, 633, L9
Ford, A. B., Davé, R., Oppenheimer, B. D., et al. 2014, MNRAS, 444, 1260
Glidden, A., Cooper, T. J., Cooksey, K. L., Simcoe, R. A., & O'Meara, J. M. 2016, ApJ, 833, 270
Gómez-Guijarro, C., Toft, S., Karim, A., et al. 2018, ApJ, 856, 121
Guillemin, P., & Bergeron, J. 1997, A&A, 328, 499
Ho, S. H., Martin, C. L., Kacprzak, G. G., & Churchill, C. W. 2017, ApJ, 835, 267
Hunter, J. D. 2007, Computing In Science & Engineering, 9, 90
Hussain, T., Muzahid, S., Narayanan, A., et al. 2015, MNRAS, 446, 2444
Johnson, S. D., Chen, H.-W., & Mulchaey, J. S. 2013, MNRAS, 434, 1765
—. 2015, MNRAS, 449, 3263
Kacprzak, G. G. 2017, in Astrophysics and Space Science Library, Vol. 430, Gas Accretion onto Galaxies, ed. A. Fox & R. Davé, 145
Kacprzak, G. G., Churchill, C. W., Barton, E. J., & Cooke, J. 2011, ApJ, 733, 105
Kacprzak, G. G., Churchill, C. W., Ceverino, D., et al. 2010, ApJ, 711, 533
Kacprzak, G. G., Churchill, C. W., Steidel, C. C., Spitler, L. R., & Holtzman, J. A. 2012, MNRAS, 427, 3029
Kacprzak, G. G., Muzahid, S., Churchill, C. W., Nielsen, N. M., & Charlton, J. C. 2015, ApJ, 815, 22
Kacprzak, G. G., Vander Vliet, J. R., Nielsen, N. M., et al. 2019, ApJ, 870, 137
Kaviraj, S. 2014, MNRAS, 440, 2944
Klypin, A. A., Trujillo-Gomez, S., & Primack, J. 2011, ApJ, 740, 102
Lam, S. K., Pitrou, A., & Seibert, S. 2015, in Proceedings of the Second Workshop on the LLVM Compiler Infrastructure in HPC, LLVM '15 (New York, NY, USA: ACM), 7:1–7:6
Lambas, D. G., Alonso, S., Mesa, V., & O'Mill, A. L. 2012a, A&A, 539, A45
—. 2012b, A&A, 539, A45
Lehner, N., Howk, J. C., Tripp, T. M., et al. 2013, ApJ, 770, 138
Lopez, S., Ellison, S., D'Odorico, S., & Kim, T.-S. 2007, A&A, 469, 61
Martin, C. L., Shapley, A. E., Coil, A. L., et al. 2012, ApJ, 760, 127
Mathes, N. L., Churchill, C. W., Kacprzak, G. G., et al. 2014, ApJ, 792, 128
Muzahid, S. 2014, ApJ, 784, 5
Muzahid, S., Kacprzak, G. G., Charlton, J. C., & Churchill, C. W. 2016, ApJ, 823, 66
Muzahid, S., Kacprzak, G. G., Churchill, C. W., et al. 2015, ApJ, 811, 132
Navarro, J. F., Frenk, C. S., & White, S. D. M. 1996, ApJ, 462, 563
Nelson, D., Kauffmann, G., Pillepich, A., et al. 2018, MNRAS, 477, 450
Nielsen, N. M., Churchill, C. W., Kacprzak, G. G., Murphy, M. T., & Evans, J. L. 2015, ApJ, 812, 83
—. 2016, ApJ, 818, 171
Nielsen, N. M., Kacprzak, G. G., Muzahid, S., et al. 2017, ApJ, 834, 148
Nielsen, N. M., Kacprzak, G. G., Pointon, S. K., Churchill, C. W., & Murphy, M. T. 2018, ArXiv e-prints, arXiv:1808.09562
Oliphant, T. E. 2007, Computing in Science & Engineering, 9, 10
Oppenheimer, B. D., Davé, R., Kereš, D., et al. 2010, MNRAS, 406, 2325
Oppenheimer, B. D., Segers, M., Schaye, J., Richings, A. J., & Crain, R. A. 2018, MNRAS, 474, 4740
Oppenheimer, B. D., Crain, R. A., Schaye, J., et al. 2016, MNRAS, 460, 2157
Ownsworth, J. R., Conselice, C. J., Mortlock, A., et al. 2014, MNRAS, 445, 2198
Peeples, M. S., Corlies, L., Tumlinson, J., et al. 2018, ArXiv e-prints, arXiv:1810.06566
Pérez, F., & Granger, B. E. 2007, Computing in Science and Engineering, 9, 21
Pointon, S. K., Kacprzak, G. G., Nielsen, N. M., et al. 2019, ApJ, submitted
Pointon, S. K., Nielsen, N. M., Kacprzak, G. G., et al. 2017, ApJ, 844, 23
Prochaska, J. X., Weiner, B., Chen, H.-W., Mulchaey, J., & Cooksey, K. 2011, ApJ, 740, 91
Putman, M. E., Peek, J. E. G., & Joung, M. R. 2012, ARA&A, 50, 491
Qu, Y., Di Matteo, P., Lehnert, M. D., & van Driel, W. 2011, A&A, 530, A10
Rubin, K. H. R., Prochaska, J. X., Koo, D. C., & Phillips, A. C. 2012, ApJ, 747, L26

Rubin, K. H. R., Prochaska, J. X., Koo, D. C., et al. 2014, ApJ, 794, 156

Savage, B. D., Kim, T.-S., Wakker, B. P., et al. 2014, ApJS, 212, 8

Schaye, J., Crain, R. A., Bower, R. G., et al. 2015, MNRAS, 446, 521

Sheinis, A. I., Bolte, M., Epps, H. W., et al. 2002, PASP, 114, 851

Shen, S., Madau, P., Aguirre, A., et al. 2012, ApJ, 760, 50

Simard, L., Willmer, C. N. A., Vogt, N. P., et al. 2002, ApJS, 142, 1

Steidel, C. C., Kollmeier, J. A., Shapley, A. E., et al. 2002, ApJ, 570, 526

Stern, J., Hennawi, J. F., Prochaska, J. X., & Werk, J. K. 2016, ArXiv e-prints

Stewart, K. R., Kaufmann, T., Bullock, J. S., et al. 2011, ApJ, 738, 39

Stocke, J. T., Keeney, B. A., Danforth, C. W., et al. 2013, ApJ, 763, 148

Strickland, D. K., & Heckman, T. M. 2009, ApJ, 697, 2030

Trujillo-Gomez, S., Klypin, A., Primack, J., & Romanowsky, A. J. 2011, ApJ, 742, 16

Tumlinson, J., Peeples, M. S., & Werk, J. K. 2017, ARA&A, 55, 389

Tumlinson, J., Thom, C., Werk, J. K., et al. 2011, Science, 334, 948

van de Voort, F. 2017, in Astrophysics and Space Science Library, Vol. 430, Gas Accretion onto Galaxies, ed. A. Fox & R. Davé, 301

Werk, J. K., Prochaska, J. X., Cantalupo, S., et al. 2016, ApJ, 833, 54

Wolf, C., Meisenheimer, K., Rix, H.-W., et al. 2003, A&A, 401, 73